ELSEVIER

Contents lists available at ScienceDirect

### Global and Planetary Change

journal homepage: www.elsevier.com/locate/gloplacha



#### Research article

# Modeling the Late Pliocene with AWI-CM3 as a contribution to PlioMIP3 core experiments<sup>☆</sup>

Fernanda DI Alzira Oliveira Matos <sup>a</sup>, Christian Stepanek <sup>a</sup>, Sven Harig <sup>a</sup>, Jan Streffing <sup>a</sup>, Qiong Zhang <sup>b</sup>, Zhenqian Wang <sup>c</sup>, Katherine Power <sup>b</sup>, Tido Semmler <sup>a,d</sup>, Dmitry Sidorenko <sup>a</sup>, Patrick Scholz <sup>a</sup>, Sergey Danilov <sup>a</sup>, Paul Gravis <sup>f</sup>, Gerrit Lohmann <sup>a,e</sup>

- <sup>a</sup> Alfred Wegener Institute, Helmholtz Centre for Polar and Marine Research, Klussmannstrasse 3, Bremerhaven, 27570, Bremen, Germany
- <sup>b</sup> Department of Physical Geography, Stockholm University, Svante Arrhenius vag 8, Stockholm, 10691, Sweden
- <sup>c</sup> Department of Biology, University of Copenhagen, Universitetsparken 15, Copenhagen, 2100, Denmark
- <sup>d</sup> Met Eireann, Glasnevin Hill 9, Dublin, D09 Y921, Ireland
- e Institute for Environmental Physics, University of Bremen, Bremen, 28359, Germany
- f School of Geography, Earth and Atmospheric Sciences, University of Melbourne, Grattan Street, Parkville, Melbourne, Victoria 3010, Australia

#### ARTICLE INFO

#### Editor: Alan Haywood

Keywords: Climate change Late Pliocene Past warm climates PlioMIP3 AWI-CM3

#### ABSTRACT

The Late Pliocene, particularly the Marine Isotope Stage KM5c (3.205 Ma BP) has been increasingly proposed as an analog to future climate change, especially considering changes in the hydrological cycle, monsoon systems, and atmospheric and ocean warming above Pre-Industrial (1850 CE) and historical levels. The Pliocene Modeling Intercomparison Project (PlioMIP), now in its third phase (PlioMIP3), seeks to explore climate of the Pliocene based on a combination of climate model simulations and proxy data reconstructions. One of its goals is also to assess the analogy between past and future climates and to quantify climate sensitivity to Pliocene boundary conditions. This work shall help to improve climate models and their application for both past and future warm climates and to provide a paleoclimate-informed assessment of uncertainties in modeled warm climates. With this manuscript we present the PlioMIP3 core simulations for the pre-industrial control (PI) and the Late Pliocene (LP) based on the AWI Climate Model, Version 3 (AWI-CM3). This represents the first application of AWI-CM3 at tectonic timescales which necessitates more extensive adjustment of model setups than the application for recent climate. We therefore take advantage of the opportunity to also document more generally the methods we devised to generate AWI-CM3 model setups for paleoclimate research under geographies that differ from the modern reference state. AWI-CM3 simulates a Late Pliocene climate that is about 4°C warmer than the pre-industrial reference, with land warming exceeding ocean warming by a factor of 1.2. Polar amplification is particularly pronounced, with Antarctic surface air temperature anomalies exceeding 6°C while Arctic anomalies reach 4°C to 5°C. In comparison to the previous PlioMIP2, this places AWI-CM3 among the warmer ensemble members, consistent with a relatively high equilibrium climate sensitivity of ~ 4 °C. Our simulations also display an intensified hydrological cycle, with global mean precipitation increasing by 0.31 mm d<sup>-1</sup>. The ocean surface warms globally to about 3.06 °C, accompanied by contrasting salinity trends, with salinization of the North Atlantic (+3 PSU) and freshening of the Arctic (-2.5 PSU) and Indian (-1 PSU) Oceans. Additionally, the meridional overturning circulation (MOC) reorganizes, with the Atlantic MOC strengthening by about 8 Sv, the Pacific MOC remaining inactive, and the global Antarctic Bottom Water cell being substantially reduced (11 Sv weaker relative to PI). We find reduced global sea-ice extent, that is halved with respect to PI in the Southern Hemisphere, and enhanced northward ocean heat transport in the North Atlantic. Overall, AWI-CM3 reproduces the large-scale climate features of the Late Pliocene inferred from proxy records and the PlioMIP2 ensemble, while highlighting key ocean-atmosphere feedbacks shaping this warm climate.

E-mail address: fernanda.matos@awi.de (F.D.A.O. Matos).

<sup>☆</sup> This article is part of a Special issue entitled: 'PlioMIP3' published in Global and Planetary Change.

<sup>\*</sup> Corresponding author.

#### 1. Introduction

The Pliocene epoch (5.332-2.588 Ma Before Present (BP)), represents the most recent example of a globally warmer climate in comparison to the relatively cooler background of the Pleistocene (Haywood et al., 2008). It is commonly subdivided into 2 stages: (1) Early Pliocene (or Zanclean), from 5.332 - 3.60 Ma BP, and (2) Late Pliocene, (or Piacenzian), from 3.60 - 2.588 Ma BP (Dowsett et al., 2023; Raffi et al., 2020). The Pliocene has become the focus of significant efforts to study a potential time-slice past analog for future climate change and to understand model-skill and model uncertainty in warm climates (Zubakov and Borzenkova, 1988; Burke et al., 2018; Tierney et al., 2020; Burton et al., 2024). However, many questions about the climate of the Pliocene remain to be further explored. This includes, in particular, the impact of gateway configurations on tectonic-scale climate variability, an area not yet explored in a multi-model ensemble. On the side of climate reconstructions, geological records of this epoch are still scarce and demand further investment in the drilling of new cores (either ice or sediment), and capacity building for analyses of proxy data (Salzmann et al., 2013; Pound et al., 2014; Dowsett et al., 2013; Foley and Dowsett, 2019; McClymont et al., 2020a,b, 2023b,a; Feng et al., 2022; Sun et al., 2024). Climate models provide the opportunity for simulating past climates, thereby supporting the interpretation of the limited proxy record and quantitative assessment of mechanisms driving Pliocene climate patterns (Haywood et al., 2019).

In this context, the Pliocene Model Intercomparison Project (PlioMIP) has arisen in the frameworks of the Coupled Model Intercomparison Project (CMIP; Eyring et al., 2016) and the Paleoclimate Modeling Intercomparison Project (PMIP; Kageyama et al., 2018). Over the past decade, the PlioMIP project has evolved through two phases. The shift from a time-slab approach in PlioMIP1 to a time-slice approach in PlioMIP2 has significantly improved the simulation of the Pliocene climate and its comparison with geological evidence (Haywood et al., 2013, 2016). Since PlioMIP2, the community has focused on the KM5c time slice (3.205 Ma BP), situated within the mid-Piacenzian Warm Period (in PlioMIP1: mid-Pliocene Warm Period) (Haywood et al., 2010, 2011, 2013, 2016). The reasons to favor this particular interval in PlioMIP2 are not only centered around the availability of proxy records for this period, but also because its boundary conditions closely resemble those of the present day. In particular, atmospheric CO<sub>2</sub> levels and orbital configuration during KM5c are similar to modern values (Haywood et al., 2016), which facilitates the application of paleoclimate insights to future climate change research. Indeed, several recent studies have already compared Pliocene to future climate, taking advantage of the Tier 1 and Tier 2 experiments from PlioMIP2. These studies highlight common large-scale features such as polar amplification, stronger monsoons, and shifts in tropical circulation, while also emphasizing important regional differences in jet stream behavior and rainfall distribution (e.g. Sun et al., 2013, 2018; Burton et al., 2025; Zhang et al., 2025).

The current phase of the PlioMIP project, PlioMIP3, (Haywood et al., 2024), designates the mid-Piacenzian reference time-slice (KM5c) of PlioMIP2 (Haywood et al., 2016) as Late Pliocene (LP), still maintaining the KM5c as the selected time-slice to enable intercomparison with previous model results. Building on the effort of previous PlioMIP phases, PlioMIP3 aims to enhance understanding and reduce model-data discrepancies observed in the representation of Late Pliocene climate. For instance, comparison with reconstructions from the geological record indicate systematic disagreements between simulations and proxy reconstructions, with models reproducing less highlatitude warming and greater tropical warming than suggested by proxy records, resulting in a steeper simulated meridional temperature gradient than most reconstructions imply (Salzmann et al., 2013; Dowsett et al., 2013; McClymont et al., 2020a). However, such mismatches highlight uncertainties not only in model sensitivity and parameterizations but also in the proxy record itself, which is highly influenced by

seasonality, habitat depth, and proxy-specific biases (Lohmann et al., 2013; McClymont et al., 2020b; Tindall et al., 2022).

PlioMIP3 also aims at addressing further outstanding scientific questions from PlioMIP1 and PlioMIP2. The community will pursue improved understanding of differences in large scale patterns of ocean circulation and of their link to ocean gateway states, as well as the climate sensitivity to different orbital configurations and  $\rm CO_2$  forcing (Haywood et al., 2024). Such extended experiment design will help to better evaluate Pliocene as a potential analog of future climate change, fostering even more comparative studies, and to understand the importance of uncertainties in Pliocene climate forcing on model-data discord. In this respect, while introducing new simulations, PlioMIP3 retains PlioMIP2 core experiments, Pre-Industrial and Late Pliocene (formerly simulation Eoi400 in PlioMIP2), along with sensitivity experiments with varying  $\rm CO_2$  concentrations, modifications to ice sheets and paleogeography comprised in the Tier 1 and Tier 2 PlioMIP3 experiments.

In this study, we describe the methodology applied to AWI-CM3 to set up the Late Pliocene (LP) and Pre-Industrial (PI; 1850 Common Era (CE)) core experiments. We analyze LP large-scale climate patterns in comparison to the PI. While our broader objective is to perform all designated PlioMIP3 experiments, the PlioMIP3 extended, optional, and legacy experiments will be discussed in forthcoming publications.

#### 2. Model description

The third generation of the Alfred-Wegener-Institute Coupled Climate Model (AWI-CM3; Streffing et al., 2022) is utilized in this study. AWI-CM3 comprises the Finite volumE Sea-ice Ocean Model version 2.5 (FESOM2.5; Danilov et al., 2017; Koldunov et al., 2019; Scholz et al., 2019, 2022) as its ocean component, and the open-source version of the European Center for Medium Range Weather Forecast's (ECMWF) Integrated Forecast System (OpenIFS; Buizza et al., 2017) as its atmospheric component. Both models are coupled using the Ocean, Atmosphere, Sea Ice, Soil Model Coupling Toolkit, version 4 (OASIS-MCT4; Craig et al., 2017; Valcke, 2013), with atmosphereocean coupling, ocean model, and atmospheric model time steps of 120, 60, and 30 min, respectively. The model suite also includes the Runoff Mapper and the XML Input/Output Server (XIOS) as auxiliary modules to redistribute continental runoff to manage OpenIFS output (Streffing et al., 2022). The ESM-tools software package (Barbi et al., 2021, https: //esm-tools.github.io/) facilitates modeling infrastructure, including model compilation, coupling, execution of the simulations, and data postprocessing.

A full documentation of AWI-CM3 in its first version (AWI-CM3.0) is provided in Streffing et al. (2022). The model employed here is the third version of AWI-CM3 (version 3.2) that, for the first time, is used for paleoclimate applications. Furthermore, the implementation of FESOM2.5 in AWI-CM3 includes many improvements relative to its predecessor, version 2.1, that is the ocean component in AWI-CM3.0. A comprehensive description of AWI-CM3.2 model improvements in comparison to AWI-CM3.0 is available in the AWI-CM3 documentation (Streffing, 2020).

In comparison to the CMIP6 ensemble (Scafetta, 2022), AWI-CM3 can be classified as a model of medium Equilibrium Climate Sensitivity (ECS), with an ECS of  $4.04\,^{\circ}\mathrm{C}$  (Fig. 1). Additionally, if AWI-CM3 would have been included in the PlioMIP2 ensemble, it would be classified as a high ECS model, ranking 7th highest and exceeding the multi-model ensemble mean of  $3.7\,^{\circ}\mathrm{C}$  (Haywood et al., 2020).

#### 2.1. FESOM2

FESOM2.5 (FESOM2 thereafter), developed at AWI, is mainly characterized by its triangular unstructured mesh and finite-volume dynamical core that enable performance and throughput similar to traditional structured-mesh models. This advancement facilitates routine

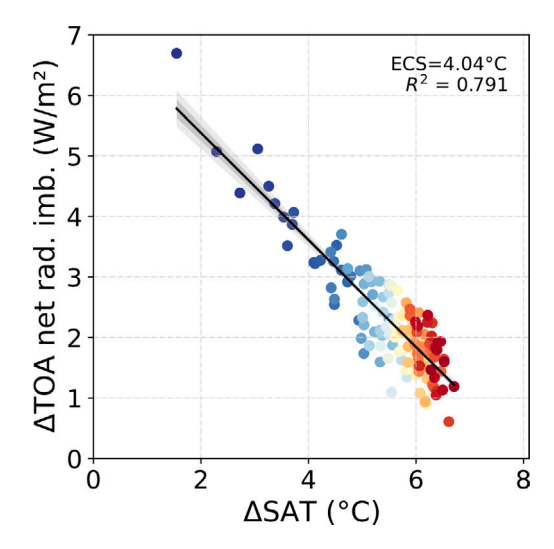


**Fig. 1.** Quantification of Equilibrium Climate Sensitivity (ECS) in AWI-CM3.2 derived via a Gregory plot (Gregory et al., 2004) representing the linear regression between the annual means of top-of-atmosphere (TOA) net-radiative imbalance and the change in global average surface air temperature (ΔSAT) under quadrupled PI  $CO_2$  concentration. Each colored dot corresponds to an annual mean value of the sample size of 150 simulation years. Colors represent the integration length of the simulation elapsed, meaning the bluer the colors, the earlier the year within the simulation and the further the model from a quasi-equilibrium. The ECS is estimated by reading ΔSAT where the trend-line meets the *x*-axis, which extrapolates global SAT anomaly to equilibrated net radiative balance, and halving that value. Uncertainty is denoted by a darker gray shade representing one standard deviation (1 $\sigma$ ) and a lighter gray shade representing two standard deviations (2 $\sigma$ ). (For interpretation of the references to color in this figure legend, the reader is referred to the web version of this article.)

application of unstructured meshes in long-term integrations required for paleoclimate research across orbital to tectonic time scales. The unstructured mesh design enables local grid refinement without nesting and allows flexible adaptation of spatial detail to accommodate boundary condition changes across timescales. The second aspect is particularly advantageous for paleoclimate simulations requiring modifications to land and sea configurations. For interpreting the results presented in this manuscript, it should be noted that the unstructured mesh approach also comes with a trade-off: the necessity of interpolation of FESOM2 model output to a common resolution when computing anomalies between simulations with differing land-sea masks (i.e., LP and PI) and therefore mesh geometries.

FESOM2 incorporates Arbitrary-Lagrangian-Eulerian (ALE) scheme, enabling the implementation of multiple vertical coordinate systems. In this sense, AWI-CM3 utilizes the  $z^*$  vertical coordinate, allowing vertical layers to move dynamically, thereby reducing spurious vertical mixing by scaling layers proportionally to sea surface height (Scholz et al., 2019). Sea-ice dynamics and thermodynamics are in FESOM2 modeled using the embedded Finite volumE Sea-Ice Model (FESIM; Danilov et al., 2015). In AWI-CM3 it prognostically calculates sea-ice surface temperature, eliminating the computation of this process in the atmospheric model (Streffing et al., 2022).

Here we employ FESOM2's standard coarse resolution ocean mesh for global applications. The PI simulation utilizes the COREII-mesh, stemming from a model setup that has been prepared for the Coordinated Ocean-ice Reference Experiments - Phase II (COREII; Large and Yeager, 2009). It consists of approximately 127,000 surface nodes and 47 vertical levels in its default PI configuration. The mesh features a nominal 1° horizontal resolution in most of the ocean interior, with higher resolution where spatial detail is key for resolving important aspects of ocean dynamics. The COREII mesh has a target resolution of

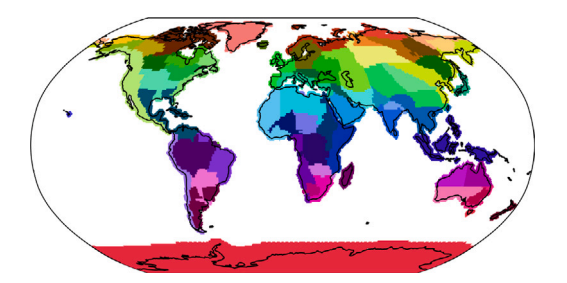


Fig. 2. River catchment map applied to OpenIFS PI control and Late Pliocene simulations. Color shading to the landside of coastlines represents catchment areas considered in the runoff mapper, whereas corresponding color shadings outside coastlines indicate the arrival and calving points of continental runoff from a specific catchment. (For interpretation of the references to color in this figure legend, the reader is referred to the web version of this article.)

1/3° near the Equator, 24 km resolution north of 50°N, and a generally higher spatial resolution near coastlines. For the LP simulation, we use a mesh generated based on the PRISM4 reconstructed Pliocene land sea mask (Dowsett et al., 2016; Haywood et al., 2016), adhering to the same resolution rules as for the standard COREII mesh. While these meshes offer a high spatial resolution in many regions, mesoscale eddies are still not dynamically resolved but parameterized via Gent-McWilliams (GM) parameterization (Gent and McWilliams, 1990). Vertical levels are discretized in increments of 5 m in the first two layers and 10 m down to 100 m depth. Below 100 m, vertical resolution decreases monotonically and inhomogeneously, reaching 350 m thickness at 6000 m depth.

#### 2.2. OpenIFS

OpenIFS in the version 43r3v2 is employed in this study in its cubic octahedral truncation TCo at wavenumber 95, corresponding to a 100 km horizontal resolution, and with 91 vertical layers (TCo95L91) (ECMWF, 2017a,b,c,d,e). An OpenIFS grid with TCo truncation was chosen as it is deemed the best choice for coupled climate and Earth System model applications (Streffing et al., 2022). OpenIFS incorporates the same physical parameterizations and dynamical core as the IFS suite, alongside the WAM (Komen et al., 1994) and H-TESSEL (Balsamo et al., 2009) models to account for atmospheric waves and land hydrology representation. The model output is handled by XIOS, accounting for interpolation and averaging of climate variables in accordance to pre-defined tables. In coupled atmosphere-ocean simulations, such as those of AWI-CM3, the global water balance is usually closed by rerouting overland excess precipitation to the ocean model. This is performed in AWI-CM3 by a runoff mapper that connects drainage and arrival points. The reference configuration divides the land surface into 66 catchments, each with catchment designated calving and arrival points (Fig. 2). To account for mass and heat flux coupling from snow falling onto ice sheets, snow that is in excess of  $10\,\mathrm{m}$  of water column depth is routed to the runoff mapper as a separate solid water flux, subsequently distributed within iceberg melt regions. The heat flux needed for melting is incorporated into the simulation's heat budget. The resulting runoff sent as a freshwater forcing to the ocean model is the sum of the solid and liquid runoffs.

The implementation of OpenIFS in AWI-CM3, contrasting with the ECHAM6 atmosphere model (Stevens et al., 2013) used in previous AWI Climate Models and Earth System Models (i.e., COSMOS, AWI-CM1.1, AWI-ESM2), enhances computational efficiency in simulating atmosphere dynamics and allows for the application of a wider range of grid resolutions, including both full and reduced Gaussian grids. This enables AWI-CM3 to employ much higher standard resolution in the atmosphere than its predecessors, and enables computationally efficient simulations at even higher spatial resolutions. Similar to

**Table 1**Centennial trends (calculated via a linear regression) and climatology over the last 200 years of the simulations.

Variable	PI	LP
2 m air temperature trends (°C per century)	0.012	0.022
TOA radiation trends (W m <sup>-2</sup> per century)	0.002	0.036
Mean TOA radiation (W m <sup>-2</sup> )	0.127	0.443
Global ocean temperature trends (°C per century)	0.019	0.071
Upper 500 m ocean temperature trends (°C per century)	0.021	0.029
Global ocean salinity trends (psu per century)	0.001	0.001
Upper 500 m ocean salinity trends (°C per century)	0.002	0.002

ECHAM6, OpenIFS features a spectral dynamic core and solutions in the grid space are derived by truncating spherical harmonics at a specific wavenumber.

# 3. Modeling the late pliocene with AWI-CM3 according to PlioMIP3 framework

#### 3.1. Experimental design

The simulations performed are named in accordance to Haywood et al. (2024) to facilitate model intercomparison within the PlioMIP3 framework. For this study, we performed two experiments spanning 700 years and 2000 years corresponding to the Pre-Industrial (PI) and Late Pliocene (LP) control, respectively. Both simulations were run until quasi-equilibrium was reached (Fig. 3), which we define as a top-of-atmosphere (TOA) radiative imbalance trend below  $0.05\,\mathrm{W\,m^{-2}}$  per century; in our case, the trend is  $0.036\,\mathrm{W\,m^{-2}}$  per century. The final 200 years of model output were used for analyses of mean large-scale climate patterns. The TOA radiative imbalance during this averaging period is  $\sim 0.443\,\mathrm{W\,m^{-2}}$ , and global mean ocean temperature trends are  $0.071\,^{\circ}\mathrm{C}$  per century for the full depth and  $0.029\,^{\circ}\mathrm{C}$  per century for the upper 500 m (Table 1). These values are comparable to, or lower than, those reported for several PlioMIP2 models (e.g. Stepanek et al., 2020; Tan et al., 2020; Zhang et al., 2021a; Williams et al., 2021).

Our PI state adheres to the PMIP4/CMIP6 piControl protocol (Eyring et al., 2016; Otto-Bliesner et al., 2017a). The PlioMIP3 LP simulation follows the protocol outlined by Haywood et al. (2024) and is consistent with the framework described for the mid-Pliocene Warm Period simulation in Haywood et al. (2016), formerly named Eoi400. While the PI simulation was branched off from an existing 500-year spinup, the LP simulation started without any preconditioning from a previous model state. Both the PI spinup and LP were initialized from climatological temperature and salinity fields provided by Polar Hydrographic Climatology, version 3.0 (PHC3.0; Steele et al., 2001), while sea ice was set to an ice-free state at the beginning of the integration, evolving dynamically under the imposed boundary conditions.

The primary difference in greenhouse gas forcing between PI and LP lies in their atmospheric  $\mathrm{CO}_2$  concentrations of 284.4 and 400 ppmv, respectively. A secondary difference is the application of PRISM4 Pliocene paleoenvironmental reconstruction enhanced boundary conditions (Dowsett et al., 2016; Haywood et al., 2016, 2024) to AWI-CM3 geography and other climatic parameters in the LP simulation. The 400 ppmv atmospheric  $\mathrm{CO}_2$  concentration chosen for the LP experiment is informed by proxy evidence and represents a best guess for the LP in PlioMIP3 and PlioMIP2 (Haywood et al., 2016). The impact of  $\mathrm{CO}_2$  concentration uncertainty on simulated LP climate is the focus of optional PlioMIP3 experiments (Haywood et al., 2016, 2024), results of which we will present in a subsequent publication. A detailed description of orbital parameters, greenhouse gas concentrations, and boundary conditions applied to each simulation is provided in Table 2.

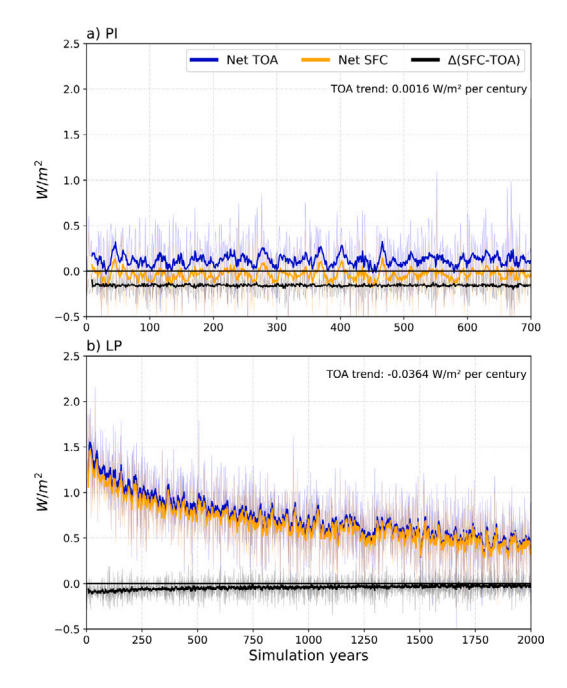


Fig. 3. Time series of the globally averaged net top-of-atmosphere (TOA), net surface (SFC) and radiative imbalance ( $\Delta$ (SFC-TOA)) for the experiments (a) PI (Pre-Industrial), and (b) LP (Late Pliocene).

Table 2
Implementation of the PlioMIP3 protocol towards derivation of AWI-CM3 PI and I.P simulations.

	PI	LP
Eccentricity	0.016764	Same as PI
Obliquity (degrees)	23.549	Same as PI
Perihelion -180	100.33	Same as PI
CO <sub>2</sub> (ppmv)	284.3	400
CH <sub>4</sub> (ppbv)	808.2	Same as PI
N <sub>2</sub> O (ppbv)	273.0	Same as PI
Aerosols	Unmodified from model	Same as PI
Land Elevation and	Unmodified from model	Anomaly as per
Land Sea Mask	modern conditions	Haywood et al.
Zura dea music	modern conditions	(2016)
Ice sheets	Unmodified from model	Prescribed as per
	modern conditions	Haywood et al.
		(2016)
Vegetation	Unmodified from model	Prescribed as per
	modern conditions	Haywood et al.
		(2016)
Soils	Unmodified from model	Prescribed as per
	modern conditions	Haywood et al.
		(2016)
Lakes	Unmodified from model	Anomaly as per
	modern conditions	Haywood et al.
		(2016)
Ocean	PHC3 climatology	Same as PI

### 3.2. AWI-CM3 adaptation to PlioMIP3 Late Pliocene boundary conditions

Haywood et al. (2016, 2024) provide guidelines for adapting preindustrial climate model configurations for the PlioMIP3 LP experiment. These guidelines were implemented in AWI-CM3 utilizing the extended boundary conditions provided in the PRISM4 dataset (Dowsett et al., 2016; Haywood et al., 2016). Paleogeographic changes relevant to the LP relative to PI conditions include significant alterations in bathymetry, land elevation, ice sheet configuration, lake, soils and vegetation. The land-sea geography displays a closed Bering Strait and Canadian Arctic Archipelago, considers opening of a West Antarctic

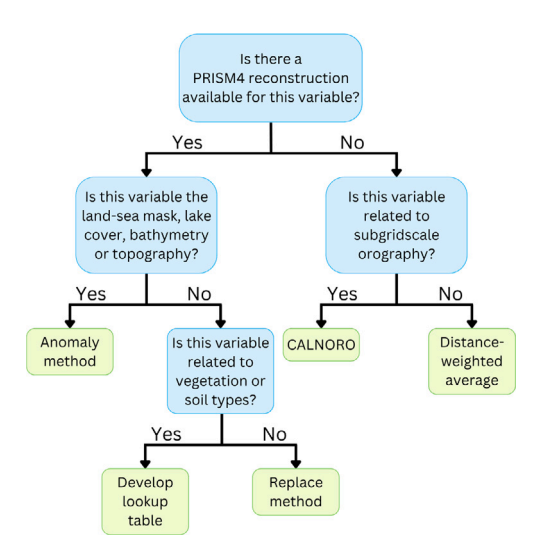


Fig. 4. Schematic of the workflow for adapting the AWI-CM3 model boundary conditions to the LP experiment. The decision tree outlines the methods used to modify variables based on their availability in the PRISM4 dataset. Blue boxes document the questions that guide the decision-making process, while boxes in green document the methods applied. (For interpretation of the references to color in this figure legend, the reader is referred to the web version of this article.)

Seaway, and modifications to the Kara Strait, South China Sea, Torres Strait and Java Sea (Fig. 5; Haywood et al., 2016). Land elevation and bathymetry adjustments account for glacial-isostatic response and mantle flow of the LP, influencing land-sea and ice sheet configurations (Raymo et al., 2011; Rowley et al., 2013). The paleo ice sheet configuration was developed based on ice sheet modeling and proxy records (Fig. 5; Koenig et al., 2015; Naish et al., 2009; Pollard and DeConto, 2009; Dowsett et al., 2010), with the Greenland Ice Sheet (GrIS) exhibiting a substantially reduced extent, particularly in its western and southern regions, according to PRISM4. The Antarctic Ice Sheet (AIS), on the other hand, is almost completely absent in its western sector (West AIS or WAIS), including the loss of the Ronne and Ross ice shelves. The eastern sector (East AIS or EAIS), however, is only reduced to reflect the loss of the Amery ice shelf and coastal glaciers, with some regions exhibiting higher elevations than present (Fig. 6). The LP vegetation distribution is derived from the PRISM3 mega-biome reconstruction (Salzmann et al., 2008), and soil and lake distributions are based on the compilation of geological evidence summarized in Pound et al. (2014).

The adaptation of AWI-CM3 boundary conditions to derive our LP simulations was conducted in five distinct phases, determined by the availability of PRISM4 reconstruction variables provided for PlioMIP (see Fig. 4). Variables considered as boundary condition in AWI-CM3 include land-sea mask (LSM), ice sheet mask, vegetation distribution (categorized in both high and low vegetation), soil types, lake cover, land elevation, and bathymetry. OpenIFS in version 43r4v2 requires a total of 56 variables, many of which are not included in the datasets provided for PlioMIP and are regarded as model initial conditions instead of boundary conditions. Fig. 4 presents a schematic representation of the decision-making process used to determine the appropriate methodology for each variable (see Sections 3.2.1 to 3.2.6).

The initial assessment involves verifying the availability of variables required as AWI-CM3 boundary conditions within the PRISM4 dataset. If available and identified as land-sea mask, lake cover, bathymetry, or land elevation, the anomaly method (see Section 3.2.1) described in Haywood et al. (2016) is implemented:

$$Model_{LP}^{var} = (PRISM4_{LP}^{var} - PRISM4_{MODERN}^{var}) + Model_{MODERN}^{var}$$

If the variable required as AWI-CM3 boundary conditions does not fall into this category, the next step is to determine whether it is related to one of the other characteristics of paleogeography for which PRISM4 provides reconstructions, specifically vegetation or soil types. For this purpose, a lookup table was developed to translate vegetation and soil types described in Pound et al. (2014) into corresponding OpenIFS boundary conditions, or simulation parameters (see Sections 3.2.3 and 3.2.4). These include the type of vegetation (low vs. high), leaf area index (LAI), vegetation cover, soil cover, and volumetric soil water content.

The ice sheet mask is prescribed directly by replacing the modern snow depth mask in OpenIFS with the interpolated PRISM4 ice sheet mask (see Section 3.2.2). For the remaining boundary conditions not directly available from the PRISM4 reconstruction, two additional methodologies are applied: variables related to sub-grid scale orography are adapted using a routine developed for the ECHAM6 atmospheric model (see Section 3.2.5). All remaining variables are corrected for LP land-sea and ice mask anomalies relative to PI using the distance-weighted average (DWA) interpolation method. Details on these methods are provided in subsequent sections, with specifics on AWI-CM3 initial and boundary conditions and adaptation methodologies for LP documented in Table A.6.

# 3.2.1. Adaptation of land elevation, bathymetry and lake cover with anomaly method

Setting up AWI-CM3 boundary conditions for the LP experiment involves a two-stage process: adapting the ocean mesh to LP conditions and configuring the atmosphere model based on the resulting ocean model land-sea mask. Implementing the LP land-sea mask modifications to the ocean model first is key to take benefit from the comparably high spatial resolution of FESOM2, facilitating detailed implementation of reconstructed LP coastlines. The anomaly method (Haywood et al., 2016, 2024) was applied to the bathymetry, land elevation, and lake cover, with bathymetry exclusively modified within FESOM2 utilizing an in-house developed mesh generation routine. The application of the anomaly method ensures that differences between Pliocene and modern geography are emphasized, while minimizing discrepancies between modern geographies across models/reconstructions (Haywood et al., 2016, 2024). Bathymetry anomalies, derived from PRISM4 boundary conditions, were incorporated into the FESOM2 mesh generation dataset, followed by interpolation and adjustment of ocean and land grid points. This procedure prevents the occurrence of both land and ocean nodes in a singular triangular mesh element, and ensures that the updated bathymetry is restricted to depths below sea level, and that the resulting LSM accurately reflects the LP reconstructed gateway changes. The LP FESOM2 ocean mesh generated with the anomaly method has a higher number of surface nodes compared to the modern COREII reference mesh (increased from approximately 127,000 to 134,288), consistent with reduced ice sheet volume and elevated sea level of approximately 24 m during the LP target time slice (Dowsett et al., 2016).

Following ocean mesh adaptation, the atmospheric model's LSM was derived by interpolating the updated FESOM2 LSM onto a regular grid. This regular grid was then interpolated onto the cubic octahedral grid of OpenIFS, replacing the existing modern land-sea mask. The transfer of the LP land-sea mask from FESOM2 to OpenIFS was facilitated by the OCP-Tool2 (OpenIFS Coupling Preparation Tool version 2; Streffing, 2021). In addition to generating a consistent LSM for OpenIFS, this tool also generates OASIS3-MCT4 input files that enable seamless coupling between AWI-CM3's ocean and atmosphere components. The AWI-CM3 LP land-sea configuration and lake distribution are shown in Fig. 5 for the LP and PI experiments, respectively. Their anomaly is also displayed in Fig. A.23 for further reference.

Similarly to the generation of new bathymetry for the ocean mesh, the PRISM4 land elevation anomalies (as elevation above sea level; Fig. 6) and lake cover were added into the modern land elevation and lake

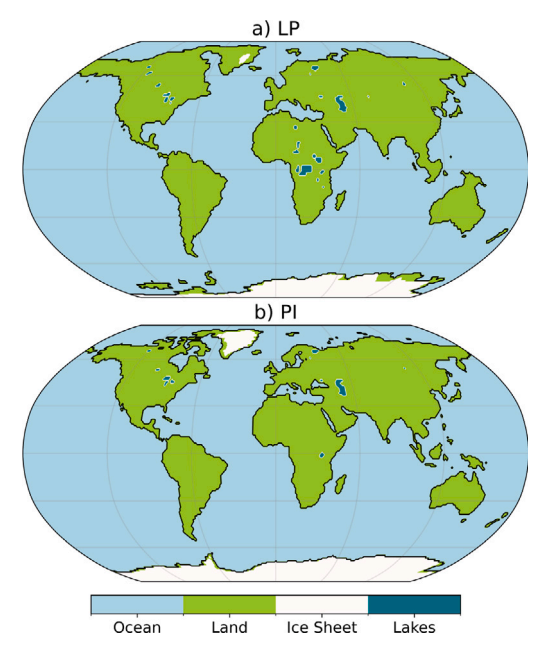


Fig. 5. Land-sea, ice, and lake masks of the (a) LP adapted from Dowsett et al. (2016), Haywood et al. (2016) and (b) PI native to the modern geography in AWI-CM3. The ocean is represented in light blue, the land in green, the ice sheet in white, and the lakes in dark cyan. (For interpretation of the references to color in this figure legend, the reader is referred to the web version of this article.)

fields of OpenIFS. Additionally, we ensured that the updated variables were physically consistent. Bathymetry (land elevation) values were adjusted to represent only elevation above and (below) sea level, while lake distribution was converted from a percentage-based representation in PRISM4 to a binary mask (0 and 1). Relative to the PI (Fig. 6b) state, the remaining areas of the EAIS exhibits elevations 250–500 m higher in LP (Figs. 6a and c), alongside a general increase in height across existing mountain ranges.

#### 3.2.2. Adaptation of ice sheet mask with field replacement

In OpenIFS, the ice sheets are implicitly defined as snow depth below 10 m and are fixed. Therefore, the snow depth mask (ice sheet mask thereafter) is fully prescribed and, as in other models without ice sheet dynamics, remains fixed in both elevation and spatial extent during model runtime.

For these experiments, the standard snow depth mask was replaced with a mask derived from the PRISM4 dataset, interpolated to the model's native resolution (Fig. 5). Resultant ice sheet orography changes were incorporated through modifications to land elevation and sub-grid scale orography fields, as detailed in Sections 3.2.1 and 3.2.5.

# 3.2.3. Adaptation of vegetation type, vegetation cover and leaf area index using a lookup table

Vegetation within our experimental setup is fully prescribed. The land component of OpenIFS classifies vegetation into 20 types according to the Biosphere-Atmosphere Transfer Scheme (BATS) model (Yang and Dickinson, 1996): ten low vegetation types, six high vegetation, and four non-vegetated land surface types (deserts, ice caps and glaciers, inland water and ocean). For our LP simulation, we followed the translation of vegetation types from the paleoenvironmental reconstruction Salzmann et al. (2008) to OpenIFS as described in Zhang et al. (2021a), considering deserts as semideserts (Table 3). A comparison of the resulting LP vegetation in AWI-CM3 with pre-industrial vegetation distribution reveals notable differences (Fig. 7). Seven vegetation types present in the pre-industrial climate are absent in our translated LP

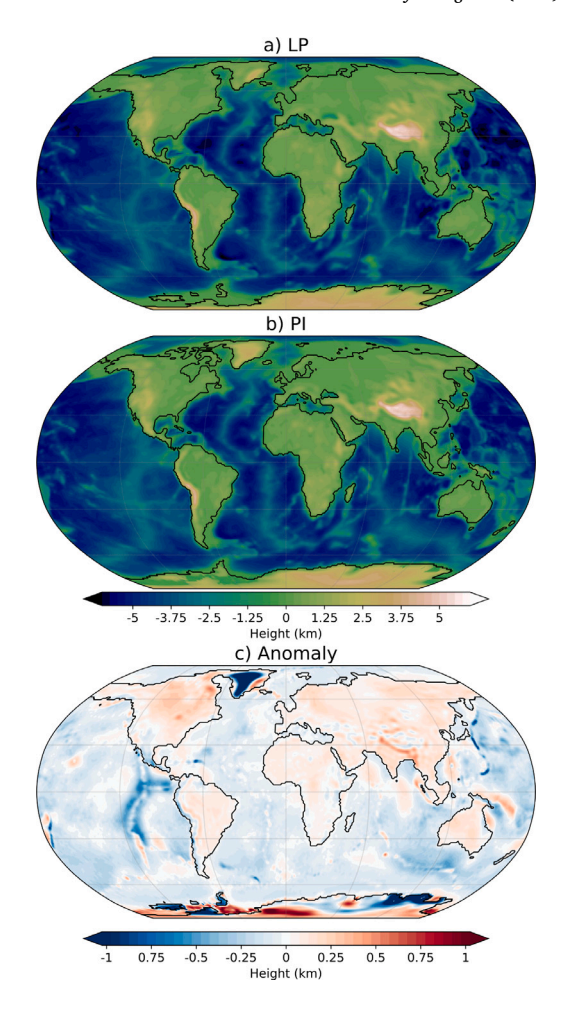


**Fig. 6.** Bathymetry and land elevation (km) of the model AWI-CM3 configured for PlioMIP3 (a) LP and (b) PI simulations. In (c) is the global anomaly between the LP and PI boundary conditions after adjustments and corrections. Positive values (red) indicate higher elevation or shallower bathymetry in the LP, and negative values (blue) indicate lower elevation or deeper bathymetry. (For interpretation of the references to color in this figure legend, the reader is referred to the web version of this article.)

version of the PRISM4 vegetation mask: Desert, Irrigated Crops, Bogs and Marshes, Evergreen Shrubs, Mixed Forest, Interrupted Forrest, and Deciduous Shrubs. Direct comparison shows an extensive expansion of needleleaf trees at high latitudes and eastern Europe, alongside deciduous broadleaf trees in temperate regions (Figs. 7a and b). Together, these two types dominate areas largely occupied by mixed and interrupted forests in the PI period. Evergreen broadleaf trees are predominant in the LP tropics and subtropics. In contrast, the distribution of low vegetation types during the LP is more scattered around the globe (Figs. 7c and d). Semidesert is widespread, while short grasses are predominant in the tropics and arid to semi-arid regions. Tall grasses, conversely, occupy regions characterized in the PI period by savannahs, shrubs, and bogs and marshes. Finally, tundra vegetation retreats northward, staying confined to the coastlines.

OpenIFS also accounts for the fraction of vegetation cover and Leaf Area Index (LAI). In our setup, we adopted the vegetation fractions outlined in Haywood et al. (2010). Unlike the standard OpenIFS configuration, where vegetation cover is expressed as a fractional value ranging from 0 to 1, our vegetation cover is defined using absolute values (Fig. A.24). LAI values from Haywood et al. (2010) were not adopted, based on the observation that LAI values are relatively consistent within each vegetation type. LAI values were extracted for all

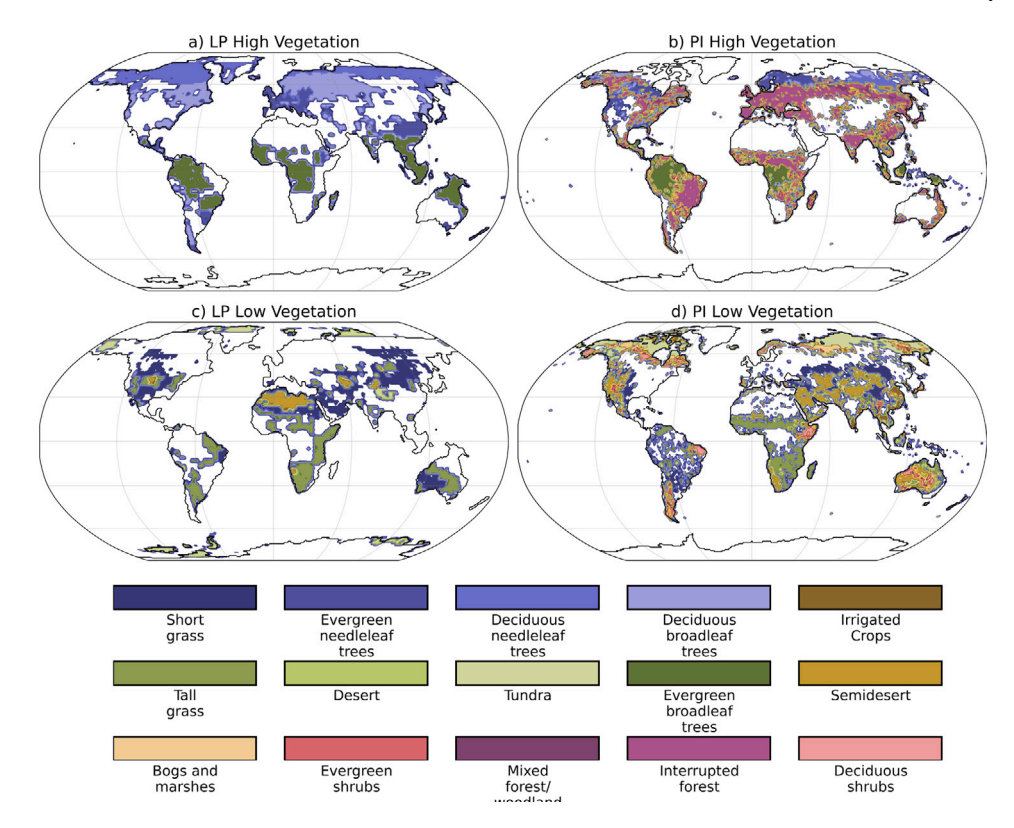


Fig. 7. Prescribed vegetation types for the PlioMIP3 LP and PI experiments with AWI-CM3, following the model original naming convention after translation using the lookup table from Zhang et al. (2021a). (a, b) High vegetation and (b, c) low vegetation. (a, c) LP and (b, d) PI.

Table 3
Translation of the PRISM4 reconstructed mega-biomes (Salzmann et al., 2008) to OpenIFS vegetation type, cover and Leaf Area Index.

PRISM4 reconstructed mega-biome	PRISM4 vegetation type	OpenIFS translation (Zhang et al., 2021a)	Vegetation cover (Haywood et al., 2010)	Leaf area index
Tropical Forest	High	Evergreen broadleaf trees	0.95	6.44
Warm-Temperate Forest	High	Evergreen needleleaf trees	0.95	5.90
Savanna and Dry Woodland	Low	Tall grass	0.90	3.79
Grassland and Dry Shrubland	Low	Short grass	0.87	2.92
Desert	Low	Semidesert	0.10	3.11
Temperate Forest	High	Deciduous broadleaf trees	0.95	5.97
Boreal Forest	High	Deciduous needleleaf trees	0.925	4.89
Tundra	Low	Tundra	0.40	2.95
Dry Tundra	Low	Tundra	0.40	2.95
Marine Core	None	Not vegetation	0	
Land Ice	None	Not vegetation	0	
No Biome Reconstruction	None	Not Vegetation	0	

grid cells associated with each vegetation type from the translation lookup table, with the maximum value assigned as the characteristic LAI (Fig. A.25). Table 3 provides a complete translation of vegetation types, vegetation cover and LAI adopted in the adaptation of AWI-CM3 for simulating the LP climate.

## 3.2.4. Adaptation of soil types and soil moisture within soil layers using a lookup table

Soil types within the PRISM4 dataset are derived from the Pound et al. (2014) reconstruction. However, implementing the paleoenvironmental reconstruction for soil types as a boundary condition is not straight-forward as the paleosol classifications in the PRISM4 do not directly align with the OpenIFS soil types. Furthermore, soil albedo is not considered by AWI-CM3 as a boundary condition. To enable translation of PRISM4 soil types to OpenIFS soil types in our simulations, PRISM4 soil textures were analyzed and compared with modern OpenIFS soil type field textures. Correspondences between PRISM4 textures and their nearest OpenIFS equivalents were established by evaluating texture ranges at each OpenIFS model grid point. This

resulted in the definition of four representative soil types for the LP simulation (Table 4). Fig. 8 displays the resulting spatial distribution of soil types for both the LP and PI simulations. Notably, the "very fine" and "organic" soil types appear exclusively in the PI configuration.

Overall, our translation captures the main shifts in soil distribution described by Pound et al. (2014), correlating with LP vegetation changes. Medium-type soil predominates across high latitudes of the Northern Hemisphere, consistent with the northward displacement of boreal temperate forests and tundra (Salzmann et al., 2008), likely representing a mixture of Gelisols and Alfisols. A confined area of coarse soil in the Kara Sea region aligns with Spodosols. Although medium-type soils are also predominant in temperate North America and Asia, terrestrial records primarily associate these with Mollisols, rather than Gelisols and Alfisols (Pound et al., 2014).

In central North America, North Africa, western Australia, and other smaller regions, our translation suggests the presence of coarse-type soil. We hypothesize these represent only Aridisols, supported by climatic evidence of a drier LP in these regions that favored the development of semi-arid and arid conditions (Zhang et al., 2024).

Table 4
Translation of the PRISM4 reconstructed soil types (Pound et al., 2014) to OpenIFS soil types.

	71	
Soil type	PRISM4 texture	Translation
Gelisol	Medium	Medium
Histosol	Fine	Medium Fine
Spodosol	Medium/Coarse	Coarse
Oxisol	Fine/Medium	Medium Fine
Vertisol	Fine	Fine
Aridisol	Coarse	Coarse
Ultisol	Fine/Medium	Medium Fine
Mollisol	Medium	Medium
Alfisol	Medium	Medium
Ice	Coarse	Coarse
Ocean	Not soil	Not Soil

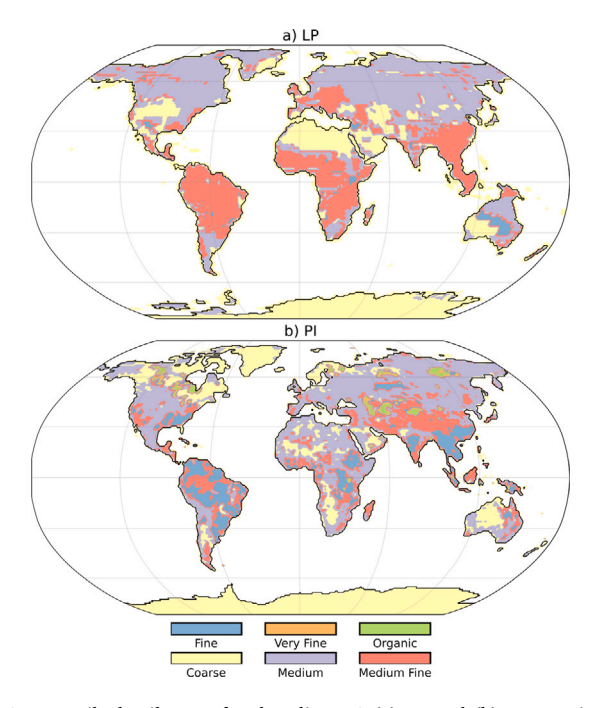


Fig. 8. Prescribed soil types for the PlioMIP3 (a) LP and (b) PI experiments with AWI-CM3, following OpenIFS conventions.

Medium-fine-type soils are predominant in central to northern South America, eastern Europe, central to western Africa, and southeast Asia. This spatial pattern aligns with records showing extensive distribution of Ultisols in southeast China, a mixture of Ultisols and Oxisols in South America, Ultisols and Histosols combinations in eastern Europe, and Oxisols in western Africa. Fine-type soils occur sparingly, primarily in central North America, Australia, and eastern Africa, mostly associated with Vertisols.

Compared to our PI soil distribution, LP soils are coarser in regions that later became agricultural centers during the Common Era (e.g., central South America, Europe, and central to southeast Asia) and those dominated by boreal forest at middle to high latitudes.

In addition to soil type, we also translated the volumetric water moisture, in units of  $m^3\,m^{-3}$  (ratio of the volume of water in cubic meters to the volume of soil in cubic meters) for each soil layer. This variable is dependent on the associated soil texture and calculated in OpenIFS as the difference between the soil field capacity and the permanent wilting point (ECMWF, 2017c). Using our lookup table, we extracted values from all grid cells within each soil texture category and computed the average soil moisture per layer. The final translation table, detailing the soil textures and corresponding layer-averaged water content, is provided in Table A.7.

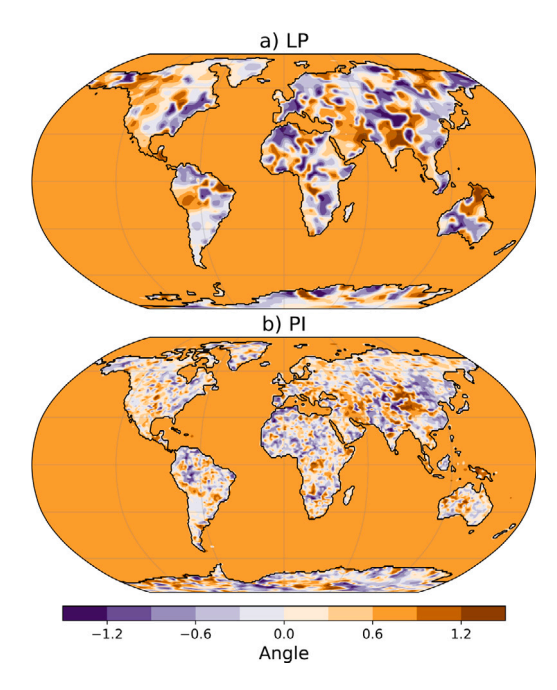


Fig. 9. Angles of sub-grid scale orography in (a) the LP and (b) the PI experiments, generated with CALNORO.

#### 3.2.5. Adaptation of subgrid-scale orography with CALNORO

The sub-grid scale orography parameters included in OpenIFS were updated from their modern field using the Subgrid Scale Orographic Parameterization (SSOP) implemented to the model ECHAM6 via the CALNORO routine, based on methods used in earlier ECHAM versions (Roeckner et al., 2003; Lott and Miller, 2013; Lott, 1999). These parameters are of highlighted importance when performing LP experiments, as their adaptation significantly impact momentum transfer from the surface to the troposphere via orographic gravity waves and low-level airflow drag over sub-grid scale mountains (Miller et al., 1989).

The updated land elevation field (as elevation above the sea level) derived using the anomaly method (Section 3.2.1), was used to derive the subgrid scale parameters including standard deviation  $\mu$ , anisotropy  $\gamma$ , slope  $\sigma$ , angle (or orientation)  $\theta$ , and mean orography elevation. Due to ECHAM6's lower horizontal resolution (T63L47) compared to OpenIFS (TCo95L91), these parameters were derived at a coarser resolution (approximately 1.9°) and subsequently interpolated to the OpenIFS native grid for the LP experiment.

Fig. 9 illustrates the LP (Fig. 9a) and PI (Fig. 9b) angles of the subgrid scale orography, representing the angle between the main land elevation axis and the low-level wind direction (Baines and Palmer, 1990), demonstrating the loss of spatial detail inherent to this adaptation.

3.2.6. Adaptation of remaining AWI-CM3 boundary conditions with DWA

The remaining variables that require adaptation to LP conditions

(Table A.6.) were adapted using inverse dictance weighting interpole.

The remaining variables that require adaptation to LP conditions (Table A.6) were adapted using inverse distance weighting interpolation (Shepard, 1968) via the *remapdis* function in CDO2.4.0 (Climate Data Operators; Schulzweida, 2023), employing 50-neighbor radius. For our adaptation, we derived three masks consisting of (1) added points (ocean to land); (2) drowned points (land to ocean); and (3) reduced ice points (land/ocean). Interpolation was applied selectively based on these masks, ensuring that new land (ocean) points were interpolated only from surrounding land (ocean) points.

Please note that we have decided to perform the DWA methodology to the remaining variables of the OpenIFS initial and boundary conditions, regardless of them being activated during the simulation to avoid numerical instabilities arising from land-sea mask discrepancies.

#### 4. Large-scale climate patterns of the LP

Unless otherwise stated, all climatological averages and variability discussed in this section are based on the final 200 years of each simulation.

#### 4.1. Atmosphere

The temporal evolution of the LP Surface Air Temperature (SAT) during model integration illustrates adjustment of the model to imposed boundary conditions and is shown in Fig. 10a. In AWI-CM3, the LP is approximately 4°C warmer than the PI global average, with land warming exceeding ocean warming by a factor of 1.2 (Table 5). This global warming signal lies at the upper end of the PlioMIP2 ensemble range of 1.7 °C to 5.2 °C (multi-model mean of 3.2 °C; Haywood et al., 2020), indicating that AWI-CM3 produces a comparatively strong but still consistent LP warming. Polar amplification is a prominent feature, particularly in the polar Southern Hemisphere, where nearsurface warming surpasses global warming by 5.6 °C (see the columns for Antarctica in Table 5). Comparatively, the polar Northern Hemisphere exhibit warming 3.6°C greater than the global average (see the columns for the Arctic in Table 5). Such amplification is also in agreement with the PlioMIP2 ensemble (Haywood et al., 2020). Interannual to multi-centennial variability is evident across all regions. The amplitude of variability, expressed as the standard deviation of the SAT anomalies over time, exhibits distinct latitudinal dependency and similar LP variability (darker colors) compared to PI (lighter colors) (Fig. 10b). Generally, our LP simulation exhibits a significantly reduced equator-to-pole temperature gradient relative to the PI as visible from the increased vertical distance between LP and PI mean SATs with increasing latitude in the Southern Hemisphere 10b.

The analysis of the average SAT over the final 200 simulation years reveals an asymmetry in high-latitude LP warming. Fig. 11 depicts a systematically warmer LP compared to the PI period. We find substantial polar amplification, but also note that warming in the polar Southern Hemisphere is amplified in comparison to the polar Northern Hemisphere, particular for regions over the ocean up to 75°S. South of this latitude, a substantial decrease of approximately 15 °C of warming to about 8 °C cooling is observed over land. This gradient in temperature arises due to the updated LP ice-sheet configuration, characterized by a reduced WAIS and increased elevation in areas of the remaining AIS. Consequently, amplified surface warming in the polar Southern Hemisphere is largely confined to the regions below sea level. In the Northern Hemisphere, amplified land warming is particularly pronounced north of 75°N, driven by the reduced GrIS and subsequent positive feedbacks associated with sea-ice loss, prescribed vegetation shifts, and albedo reduction in this region.

Previous research on Pliocene climate highlights that only some of the PlioMIP2 models simulating the LP exhibit amplified seasonality compared to PI period whereas the ensemble mean reveal a relatively flat seasonality that might conceal regional and seasonal variability, particularly in the Northern Hemisphere (Haywood et al., 2020). Fig. 12 illustrates the annual mean (panels a and b), the boreal summer (June-July-August (JJA)), and the boreal winter (December-January-February (DJF)) anomalies in LP SATs and precipitation compared to PI. Fig. 12a confirms the strong polar amplification revealed by Figs. 10 and 11 and uncovers a substantial spatial heterogeneity in the distribution of warming. Enhanced LP warmth is evident in the Northern Hemisphere north of 30°N, in regions with modified land-sea configurations (e.g., the Canadian Arctic Archipelago, Bering Strait), and in the Arctic. In the Southern Hemisphere, amplified warming occurs in the Southern Ocean around the Sea Ice Zone (SIZ) and in regions with updated Antarctic Ice Sheet configuration, in particular in western Antarctica. Additionally, mountain ranges exhibit disproportionate warming attributed to topographic changes in the PRISM4 reconstruction (Fig. 6).

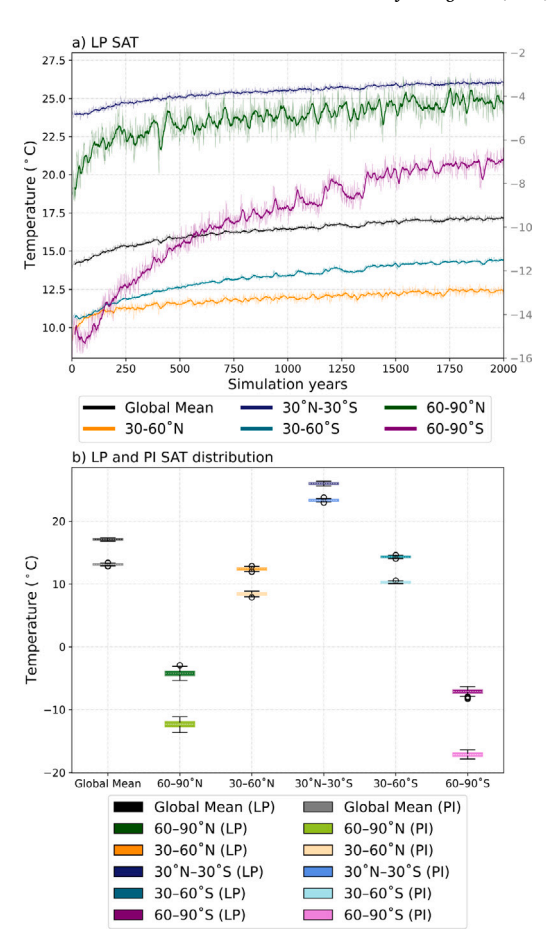


**Fig. 10.** Global and latitudinal characteristics of surface air temperature (SAT). (a) Evolution of SAT over different latitude bands and for the global mean in the LP simulation. (b) Global and latitudinal mean and variability of the SAT across different latitudinal bands of the LP (darker colors) and PI (lighter colors). In (a), a 15-year rolling mean (thicker lines) is superimposed on the annual means (thinner lines). In (a), the left *y*-axis corresponds to global (black), 30° to 60°N (orange), 30°N-30°S (dark blue) and 30° to 60°S (dark cyan) regions, while the right *y*-axis (gray) represents the polar Southern (purple) and Northern (green) hemispheres. (For interpretation of the references to color in this figure legend, the reader is referred to the web version of this article.)

Global annual precipitation anomalies (Fig. 12b) indicate a general increase in tropical and mid-latitude precipitation. Please note that we have applied a 3× 3° spatial smoothing to the Figs. 12b, d, and f to remove the wiggles near steeper topography (i.e. the Andes) arising due the spectral truncation of OpenIFS. Such smoothing was also done in Savita et al. (2024), where it was shown to not introduce any further biases to their findings. Enhanced rainfall is found particularly in monsoonal regions, consistent with an intensified hydrological cycle. Nevertheless, drier conditions are observed in southern Africa, Northeast Brazil, northwestern South America to southern North America, the Sea of Japan, and where land is exposed around Southeast Asia and the Indonesian Archipelago. Precipitation anomalies close to the equator resemble a northward shift of the Intertropical Convergence Zone (ITCZ) that has been previously described for PlioMIP2 (Han et al., 2021). Furthermore, we find a strong link between increased SAT and precipitation in the western North Atlantic, mostly during boreal winter, and enhanced precipitation over Greenland that is most pronounced in boreal summer.

Seasonally, boreal summer (JJA) exhibits stronger land surface warming in the Northern Hemisphere compared to the Southern Hemisphere (Fig. 12c), with an overall enhanced precipitation except in

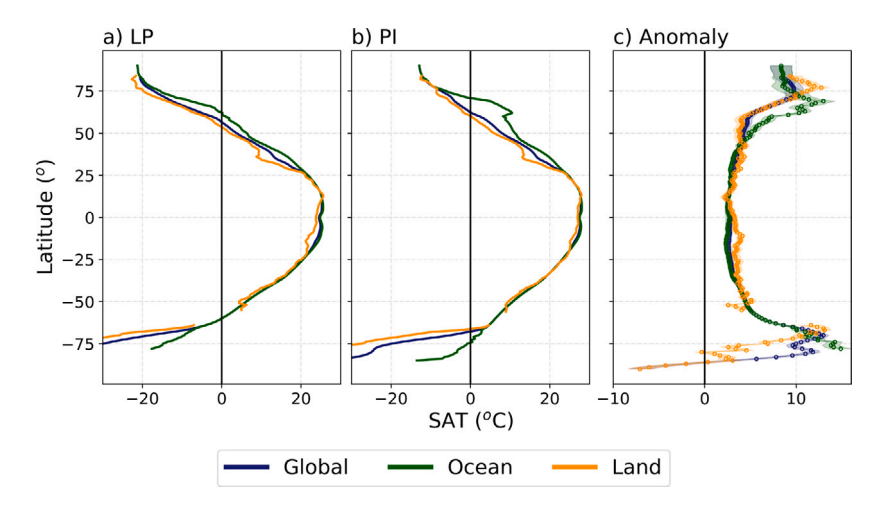


Fig. 11. Dependency of surface air temperature (SAT) on land vs. ocean and on latitude for LP and PI. Global (dark blue), land (orange), and ocean (green) zonal mean surface air temperatures shown for (a) LP and (b) PI. Substantial reduction of the meridional temperature gradient is illustrated via the anomaly between both experiments that is shown in (c). Shaded areas denote the interannual standard deviation over the final 200 simulation years. Circle markers indicate latitudes where anomalies are statistically significant at the 95% confidence level. (For interpretation of the references to color in this figure legend, the reader is referred to the web version of this article.)

Table 5 Dependency of surface air temperature (SAT) on realm (land vs. ocean) and region (global, Arctic ( $60^{\circ}$  to  $90^{\circ}$ N), Antarctic ( $60^{\circ}$  to  $90^{\circ}$ S)) for PI and LP, and the LP anomaly with respect to PI, in units of  $^{\circ}$ C.

Experiment	SAT				⊿SAT w	wrt. PI				
ID	Global	Land	Ocean	Arctic	Antarctica	Global	Land	Ocean	Arctic	Antarctica
PI	13.1	8.0	15.8	-11.9	-16.6	_	-	_	_	_
LP	17.1	12.5	19.5	-4.3	-7.0	4.0	4.4	3.8	7.6	9.6

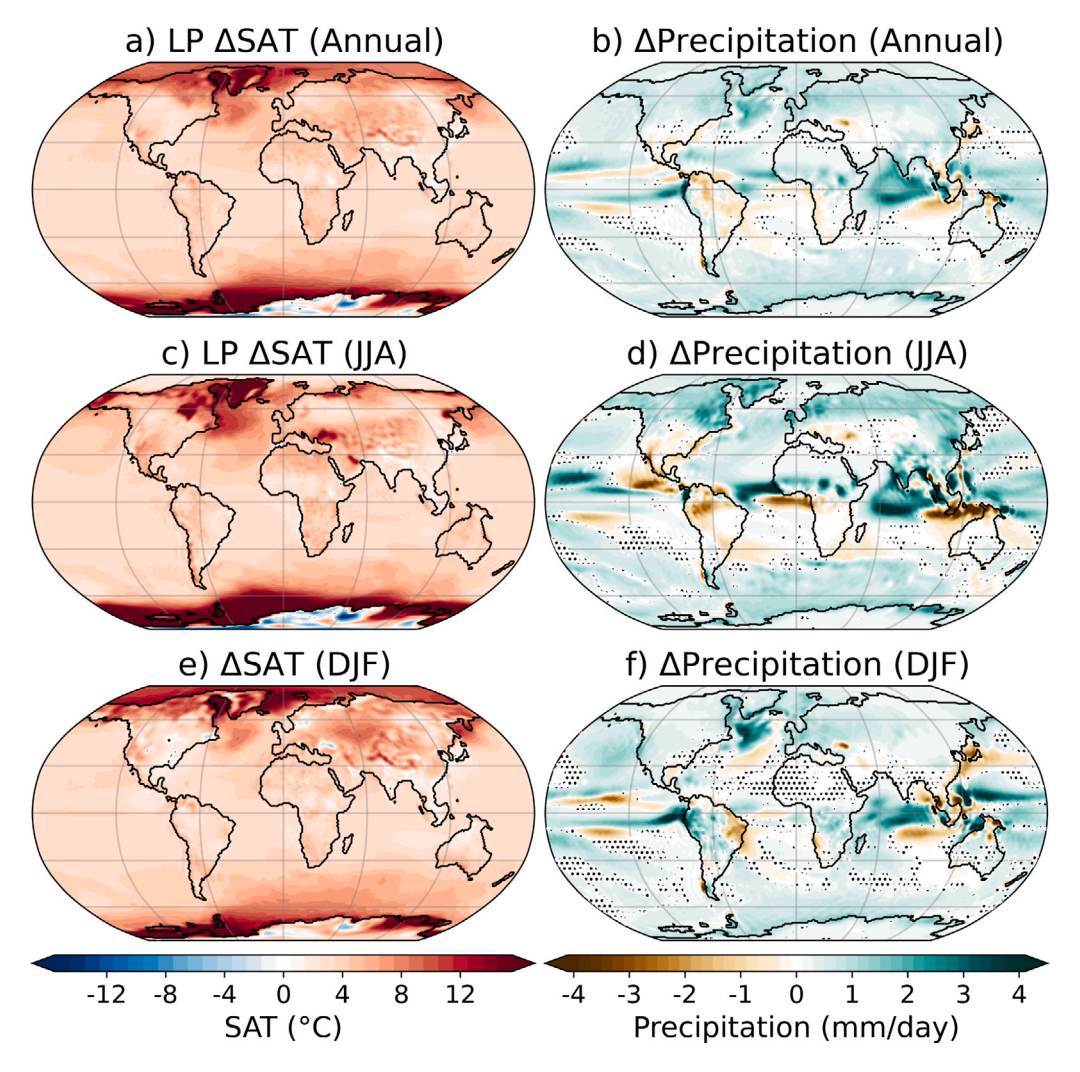
western ocean basins, and south and north of the ITCZ (Fig. 12d). During boreal winter (DJF), warming shifts northward in the Arctic, amplifies over central Asia and reduces considerably in the Southern Ocean (Fig. 12e). Precipitation patterns enhances over the central and south America, Europe, and Africa, bringing wetter conditions to the Amazon region, African savannah, and North Atlantic subtropical gyre (Fig. 12f) that were otherwise experiencing drier conditions in boreal summer (Fig. 12d). South Asia and North America, however, do not exhibit this shift, experiencing a weakened hydrological cycle from boreal summer to winter. South America is the region showing the most contrasting seasonality, with the Amazon Region and South Brazil drier during boreal summer, while being wetter during boreal winter. Additionally, Northeast Brazil and central Argentina, which did not display a significant pattern precipitation anomaly during boreal summer, become substantially drier during boreal winter.

Fig. 13 highlights regional Arctic and Antarctic warming/cooling patterns of Fig. 12 that are critical for understanding the climatic response to LP boundary conditions. As evinced by Figs. 13c, d and e, East Antarctica exhibits cooling, attributable to the elevated portions of the EAIS, which then conceals surface atmospheric warming attributed to amplified greenhouse gas forcing in the LP relative to the PI simulation in Fig. 11. This yields a multipole of warming and cooling over Antarctica, with warming focused on western Antarctica, Antarctic Peninsula, and East Antarctica north of 80°S in a region spanning Oates Land to Wilkes Land and into Queen Mary Land. Other regions east of the Transantarctic Mountains, and in particular the South Pole, are predominantly colder than PI.

In comparison, in the Arctic we find a much more homogeneous picture of LP warmth. Strongest warming is found in a south-north oriented band across the center of Greenland, influenced by reduced GrIS extent and by prescribed boreal forest (i.e. deciduous needle/broadleaf trees in Fig. 7) and tundra during the LP, with a strong seasonal amplification in boreal summer. Further regions of pronounced boreal summer

warmth are Hudson Bay and Bering Strait, where the land is exposed in simulation LP. Strong warming in boreal winter is found across the Central Arctic and in particular between Iceland and Svalbard and as well in the Labrador Sea and Baffin Bay. Below we will show that these changes towards increased Arctic SAT occur in combination with reduced Arctic sea-ice in the LP simulation, which suggests a complex interplay of different LP forcing agents related to geography and atmospheric greenhouse gas concentrations. Quantifying their individual contribution to LP high latitude SAT anomaly patterns necessitates analysis of additional LP sensitivity experiments simulated by AWI-CM3. These simulations and resulting analysis will be presented in a forthcoming publication. Overall, the global warming pattern observed in the LP simulation is generally consistent with PlioMIP2 models, with the exception of some models exhibiting regional cooling outside of Antarctica (Haywood et al., 2020).

Large-scale warming patterns (Figs. 12a, c and e, and 13) indicate substantial positive feedbacks that regionally amplify a global climate response to LP forcing, like the ice-land-albedo feedback. For instance, Fig. 14 indicates a correlation between temperature and surface albedo across diverse geographical areas. Surface albedo is predominantly lowered in LP, particularly at middle to high latitudes where we find strong boreal/austral winter warming (Figs. 12 and 13), and over regions of reduced ice sheets. Hudson Bay, that is changed to land in LP, shows reduced albedo in response to the predominance of needleleaf trees that have lower albedo in comparison to other less absorptive vegetation types. Similarly, albedo is reduced in regions of the Labrador Sea and Baffin Bay that are strongly sea-ice covered during PI. Increased albedo, that would counteract increased SAT in simulation LP, is present over the remaining land area of North and South America, Africa, and Australia (albeit at rather small amplitude). On the other hand, albedo is substantially increased in regions of the Maritime Continent, including a part of northwestern to central North America, and a substantial part of eastern to northeastern Siberia west of the river-mouth of the Amur and the Kolyma Range.



**Fig. 12.** Annual and seasonal mean (a, c, e) surface air temperature (SAT) and (b, d, f) precipitation anomalies for LP in relation to PI for the last 200 simulation years. Annual means shown in (a, b), while (c, d) shows the boreal summer (June, July, August) average, and (e, f) shows the boral winter (December, January, February) average. The overlaid black dots indicates regions the anomalies are not statistically significant (p < 0.05). (For interpretation of the references to color in this figure legend, the reader is referred to the web version of this article.)

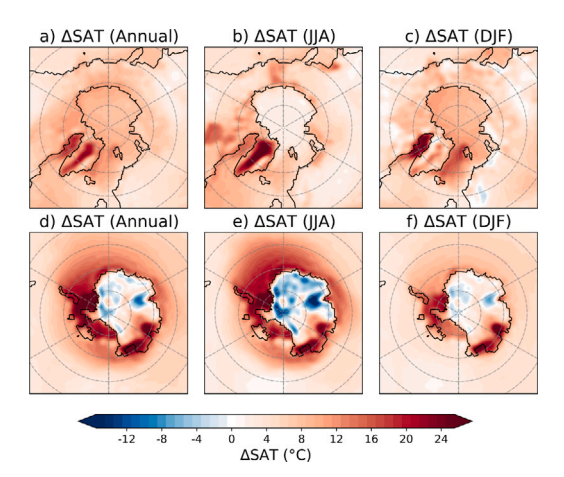


**Fig. 13.** Similar to Figs. 12 a, c, and e, but focusing on the two polar regions, featuring North Polar stereographic projection in (a, b, c), and South Polar stereographic projection in (d, e, f).

A comparison of Fig. 14 with Figs. 5, 7, and 8 shows that in the LP simulation surface albedo is altered in response to changes in icesheet configuration, soil composition, lake distribution, and vegetation cover. Lowered albedo amplifies warming in regions with the most pronounced boundary condition changes, like the Bering Strait, Canadian Arctic Archipelago, and the Southern Ocean. It is evident that much of the change in albedo patterns aligns well with land mass addition/removal and soil/vegetation updates from the PRISM4 reconstruction. Enhanced albedo over northeast Asia and northwest North America corresponds in part with expanded short grass coverage in the LP, contrasting with more absorptive forests in the PI climate. Reduced albedo in other areas is consistent with boreal deciduous forest expansion during the LP. Over the Southern Ocean, the albedo is significantly reduced at the SIZ boundary, indicating the loss of seasonal sea-ice in this region. The widespread decrease in surface reflectivity at high latitudes, induced by LP boundary conditions, results in increased net surface shortwave absorption, reinforcing warming from imposed CO2 forcing. Additionally, the close spatial resemblance between albedo anomalies and intense warming regions strongly supports the polar amplification pattern observed in Fig. 12a.

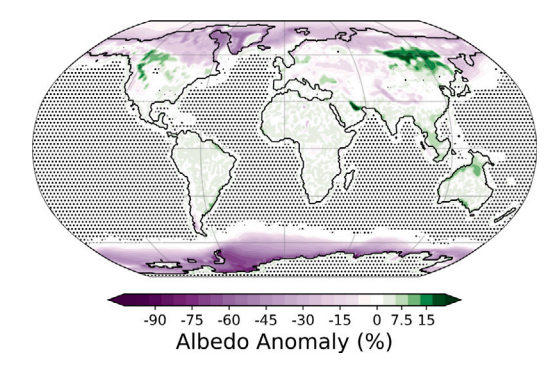


**Fig. 14.** Anomaly of the LP surface albedo in relation to PI. The overlaid black dots indicates regions the anomalies are not statistically significant (p < 0.05). (For interpretation of the references to color in this figure legend, the reader is referred to the web version of this article.)

#### 4.2. Sea-ice

The pronounced warming and reduced surface albedo at boreal high latitudes observed in the LP simulation with respect to PI (Figs. 12, 13, and 14) are closely linked to substantial sea-ice losses in the Arctic (Fig. 15). The PI simulation is characterized by >90% of sea-ice coverage across most of the central Arctic Ocean in March (Fig. 15a) and towards the Pacific and Atlantic Oceans via open Arctic gateways. In September, the sea-ice margin becomes thinner (Fig. 15c), and extensive sea-ice (>90%) is concentrated in the Amerasian Basin, whereas shallower regions, such as the Barents, Kara, and Laptev Seas, experience 40%-60% sea-ice loss relative to the PI sea-ice maximum margin. Conversely, under LP conditions, and with alterations to land cover in the Bering Strait, Canadian Arctic Archipelago, and Eurasia, sea-ice is strongly reduced and primarily confined within the central Arctic Ocean, with a clear retreat in the Greenland-Iceland-Norwegian (GIN) Seas compared to pre-industrial levels. Additionally, AWI-CM3 simulates a nearly icefree Arctic Ocean during boreal summer, characterized by a residual ice cap near the North Pole and concentrations below 30% in most sectors. This represents a 60%-80% reduction in sea-ice minimum compared to PI conditions. The seasonal pattern of Arctic sea-ice loss aligns with the 10%-15% reduction in surface albedo displayed in Fig. 14.

The LP sea-ice concentration in the Southern Hemisphere exhibits a substantial reduction relative to PI (Fig. 16). While residual sea-ice persists along the Weddell Sea and western Ross Sea coastlines during austral summer in the PI simulation (Fig. 16a), corresponding to the austral summer sea-ice minimum. However, the LP simulation indicates a near absence of austral summer sea-ice (Fig. 16b), limited primarily to the eastern Ross Sea. The removal of a significant portion of the WAIS in the LP experiment likely contributes to this extreme sea-ice reduction, as the opened West Antarctic seaway as the exposed/drowned and ice-sheet-free land masses of the opened West Antarctic seaway in LP are more absorptive than in PI. Thus, sea-ice formation is likely hampered around Antarctica through amplified local surface warming (Fig. 13). This local surface warming is supported by the approximately 90% reduction surface albedo within the SIZ surrounding the Antarctic continent (Fig. 14).

The winter sea-ice maximum also demonstrates a marked response to altered boundary conditions. The PI simulation (Fig. 16c) depicts sea-ice extending northward to approximately 60°S, covering the Ross, Weddell, and Amundsen-Bellinghausen Seas with concentrations exceeding 90%. During the LP, the SIZ retreats poleward, reaching northward of 70°S only in the Pacific Sector of the Southern Ocean, where sea-ice concentration increases by 20%. Beyond the Pacific sector, LP winter sea-ice is largely absent in the Atlantic and Indian Sectors of the Southern Ocean, restricted to the Weddell and Scotia Seas, and Prydz Bay.

The analysis of seasonal sea-ice area throughout the model runtime (Fig. 17) contextualizes spatial patterns of sea-ice concentration (Figs. 15 and 16). The time series depict the evolution of March and September sea-ice area in both hemispheres and globally for the LP experiment, as well as globally for the PI experiment. Please note that our PI simulation only spans 700 years. Consistent with Figs. 15 and 16, Fig. 17 reveals a substantial reduction in summer sea-ice area in both hemispheres under LP conditions. Near Antarctica, summer sea-ice nearly disappears by the end of the simulation, confirming the localized sea-ice loss seen in Fig. 16b. Thus, LP March sea-ice is represented almost exclusively by the Arctic, which shows substantial decline of 45% from the beginning to the end of the model simulation. The PI global sea-ice area time series (black lines) further underscore LP sea-ice loss in March and reveal weakened variability.

The LP September sea-ice area reflects contributions from both Arctic and Antarctic regions. Arctic winter maximum sea-ice area remains stable throughout the simulation. Antarctic sea-ice extent decreases from 20 million  $\rm km^2$  to approximately 6 million  $\rm km^2$ , primarily due to the substantial reduction in sea-ice cover within the Atlantic and Indian sectors of the Southern Ocean. This decline is not offset by increased sea-ice presence around  $\rm 60^{\circ}S$  in the Pacific Sector of the Southern Ocean (Fig. 16d).

#### 4.3. Ocean

### 4.3.1. Sensitivity of oceanic thermohaline properties to modified boundary conditions

The LP experiment reveals a surface ocean response to modified boundary conditions consistent with properties of the large-scale atmospheric changes (Fig. 12). The sea surface temperature (SST) exhibit an overall positive temperature anomaly (Fig. 18a), except in the Sea of Japan. The global mean ocean surface warming with respect to PI of 3.06 °C, as in the atmosphere, falls within the upper end of the PlioMIP2 ensemble (mean of 2.6 °C Weiffenbach et al., 2024), particularly due to an amplified warming in the North Atlantic, Nordic Seas, North Pacific, and the Atlantic and Indian Ocean sectors of the Southern Ocean, with temperature anomalies exceeding 4 °C. These regions correlate with regions of maximal atmospheric warming and surface albedo reduction over adjacent continents and sea-ice zones (Figs. 12a and 14), indicating robust ocean-atmosphere coupling. Specifically, in the North Atlantic, diminished snow and sea-ice cover (Fig. 15) are linked to enhanced surface heat absorption, which is reflected in intense SST warming within the Labrador Sea, Barents Sea, Baffin Bay and along the eastern North American coastline.

In the Southern Hemisphere, SST increases around Antarctica, aligning with pronounced atmospheric warming over the Southern Ocean (Fig. 12a), particularly in the Atlantic and Indian sectors, where sea-ice loss is also most pronounced (Fig. 16d). The Sea Surface Salinity (SSS) anomalies (Fig. 18b) suggest a response of regional hydrological and cryosphere dynamics to imposed boundary conditions. Extensive surface freshening is observed across the northernmost part of the Central Arctic Ocean, in the subtropical gyre of the Indian Ocean, and tropical western Africa at the Niger river mouth. We find pronounced regional extrema of reduced SSS across the Mediterranean Sea and in the Sea of Japan, indicative of increased freshwater input from precipitation, river runoff, and potential sea-ice and glacier melt, depending on the region. The presence of LP megalakes in central Africa inferred from the proxy record (Pound et al., 2014), coupled with wetter austral summer conditions, results in enhanced river runoff in western Africa. Conversely, salinization of the North Atlantic subpolar gyre and the Laptev, East Siberian, and Chukchi Seas can be partially attributed to the elimination of flow through the Bering Strait and Canadian Arctic Archipelago and restricted transport through the Kara Strait.

The restricted flow that supports salinization then counteracts buoyancy gain due to extensive warming in the North Atlantic, which sustains deep convection, albeit more confined to the Labrador and

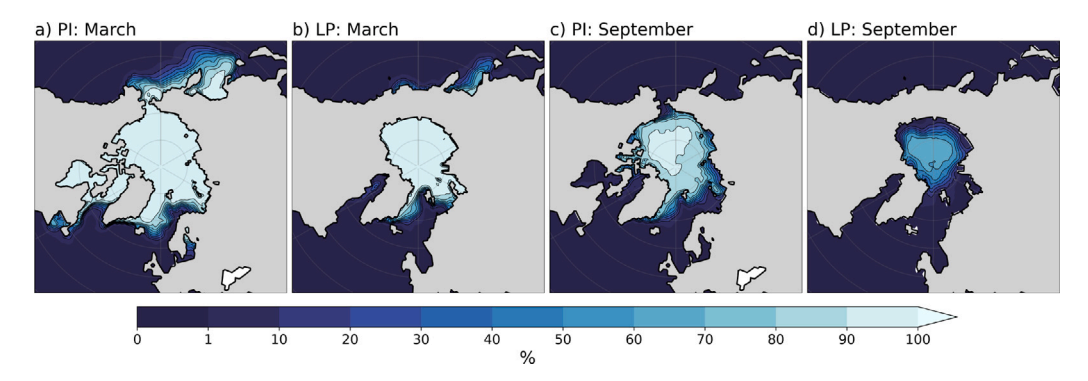


Fig. 15. Arctic March (a, b) and September (c, d) sea-ice concentration for the PI (a, c) and LP (b, d) averaged over the last 200 simulation years.

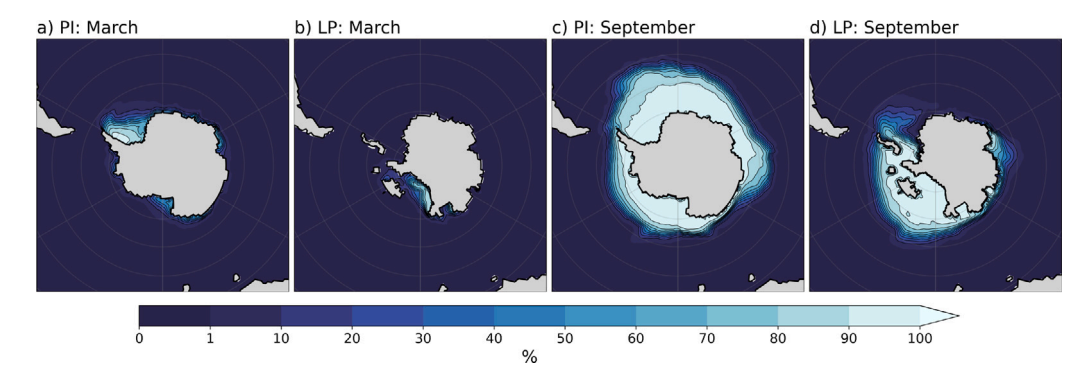
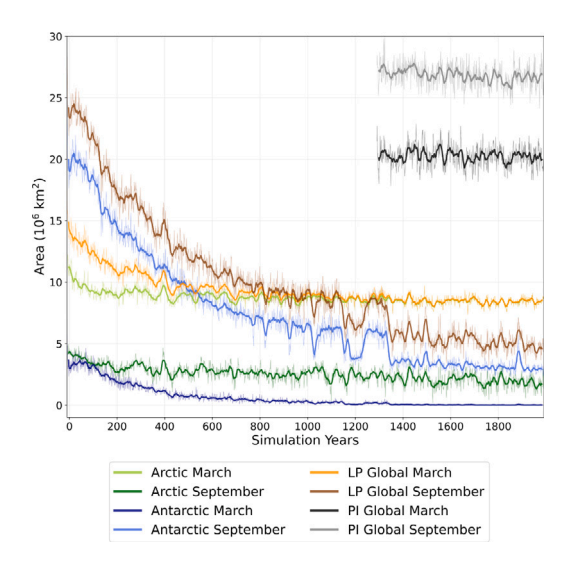


Fig. 16. Antarctic March (a, b) and September (c, d) sea-ice concentration for the PI (a, c) and LP (b, d) averaged over the last 200 simulation years.



**Fig. 17.** Temporal evolution of the Sea Ice Area for LP and PI simulations. Arctic and Antarctic shown for LP only, while global averages are presented for both LP and PI. September (March) relates to the minimum (maximum) Arctic (Antarctic) Sea Ice Area. Baseline levels of the PI Global March and September Sea Ice Area are represented in black and gray, respectively, for direct comparison. (For interpretation of the references to color in this figure legend, the reader is referred to the web version of this article.)

Greenland-Iceland-Norwegian (GIN) Seas (Fig. B.26b). This shift in deep convection sites is consistent with multiple studies that indicate their reorganization in warmer climates (Lique and Thomas, 2018; Gou et al., 2024; Chafik and Rossby, 2019; Årthun et al., 2023). A similar pattern of salinization despite the overall ocean warming is seen in the Southern Ocean, especially in the Ross and Weddell Seas, where deep convection typically occurs (Orsi et al., 1999), although

the magnitude of warming surpasses the salinization and inhibits deep convection (Fig. B.26d). These surface anomalies (Fig. 18) indicates that the paleogeography of the LP likely modulates and sustains LP warmth via maintenance of a strong thermohaline circulation and ocean heat transport in the North Atlantic (Otto-Bliesner et al., 2017b; Weiffenbach et al., 2023).

Our LP simulation demonstrates rapid surface ocean temperature increase within the first 500 years (Fig. 19a) followed by gradual equilibration. Surface warming exceeds 3 °C relative to PI levels, consistent with amplified SST patterns (Fig. 18a) and the associated feedbacks driven by reduced sea-ice cover (Figs. 15 and 16). However, while the surface ocean of the LP simulation reaches quasi-equilibrium, the deeper ocean continues to warm (Fig. 19a), indicating ongoing deep ocean heat uptake despite surface stabilization. Salinity evolution displays non-linear behavior (Fig. 19b). Surface freshening, consistent with intensified Arctic and continental marginal sea freshening (Fig. 18b), does not penetrate to subsurface and deeper levels, where salinity gradually increases. Therefore, deep ocean salinization, contrasting with surface freshening and warming, implies increased water column stratification. Note that Fig. 19 displays global averages, and upon inspecting Fig. 18b, it is likely that the surface Atlantic Ocean time evolution shows an upper ocean salinization trend, rather than freshening.

### 4.3.2. Overturning circulation in the LP

The large-scale adjustments in temperature, salinity, and sea-ice, as detailed in Sections 4.2 and 4.3, culminate in a substantial reorganization of the global overturning circulation under LP boundary conditions. Fig. 20 illustrates the meridional overturning streamfunction for the global, Atlantic, and Pacific basins under PI (Figs. 20a, b and c) and LP (Figs. 20d, e, and f) climates, respectively.

In the Atlantic basin, the PI simulation's (Fig. 20b) Atlantic Meridional Overturning Circulation (AMOC; Fig. 20b) reaches a maximum strength of approximately 17 Sv at around 39°N and 1000 m depth. The LP simulation (Fig. 20e) displays a significant strengthening and

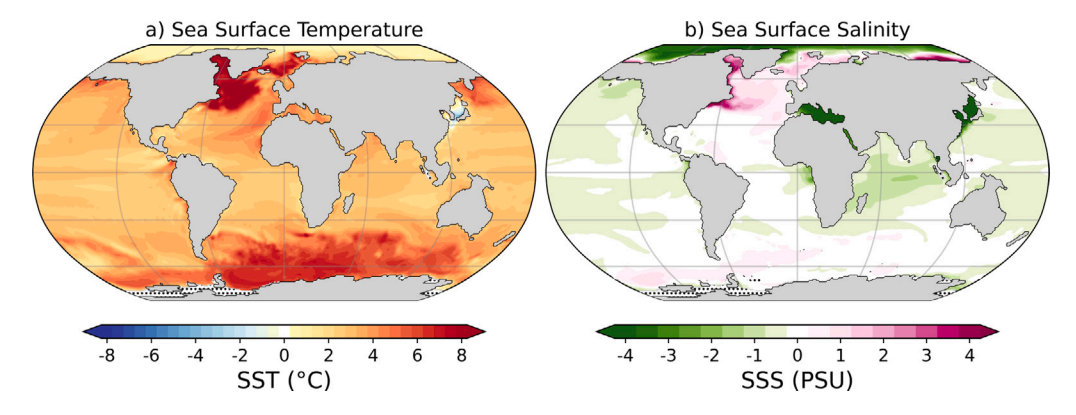


Fig. 18. Change in SST and SSS in simulation LP in relation to the reference state PI. Annual mean (a) SST and (b) SSS shown as an average for the last 200 simulation years. The overlaid black dots indicates regions the anomalies are not statistically significant (p < 0.05).

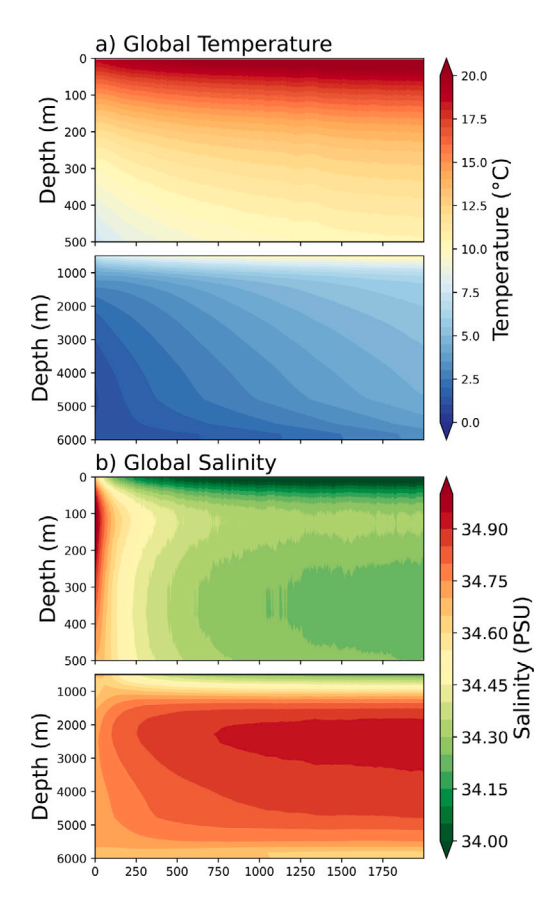


Fig. 19. Surface to deep ocean differences in the LP in comparison to PI. Shown is temporal and vertical evolution of the LP global mean seawater (a) temperature and (b) salinity. For both quantities we show conditions in the surface to subsurface ocean (uppermost  $500\,\mathrm{m}$ ) and in the deep ocean ( $500\,\mathrm{m}$  to  $6000\,\mathrm{m}$ ) separately.

deepening of the AMOC (from a maximum strength of 15 Sv to 24 Sv and depth of 2500 m to 3500 m), and intensification of the upper overturning cell, congruent with the relative salinization of the North Atlantic (Fig. 18b). Unlike the behavior for transient and quasi-equilibrium warming and freshwater hosing scenarios under modern geography, where surface freshening tend to weaken the AMOC (Stommel, 1961; Broecker, 1991; Rahmstorf, 1995; Jackson and Wood, 2018; Fox-Kemper et al., 2021; Max et al., 2022; Jackson et al., 2023; Baker et al., 2025), the LP paleogeography supports a more vigorous overturning. As discussed in Section 4.3, the stronger LP AMOC likely stems from to the closure of

the Bering Strait and the Canadian Archipelago, which limits the inflow of fresh Arctic water into the North Atlantic (Otto-Bliesner et al., 2017b; Zhang et al., 2021b; Weiffenbach et al., 2023). Consequently, the North Atlantic maintains higher salinity, sustaining surface buoyancy fluxes and interior mixing towards deep water formation at convection sites, despite overall warming and reduced sea-ice cover (Figs. 18, 15, 16, and B.26). These dynamics emphasize the need to interpret past warm periods in the context of their unique boundary conditions. As a comparison, the AMOC simulated by AWI-CM3 under the CMIP6 abrupt-4xCO2 framework shows substantially weakened and shoaled AMOC in comparison to the LP experiment (Fig. B.28), highlighting the effect of gateway changes to ocean circulation in the Atlantic.

The overturning time series (Fig. 21) confirms the robust North Atlantic deep water formation regime suggested in Fig. 20b, showing a stable and intensified AMOC throughout the LP simulation. The depth-dependent temporal evolution of the overturning circulation (Fig. B.27) further illustrates the consistently strong AMOC in the LP, with no indication of collapse.

In the Pacific basin, the PI upper overturning cell is dominated by the North Pacific Intermediate Water (NPIW) from 40° to 45°N and at around 900 m depth, while the lower overturning cell comprises the Antarctic Bottom Water (AABW), the Pacific Deep Water (PDW), and the Antarctic Intermediate Water (AAIW) (Fig. 20c and Graphical Abstract). Under LP conditions the PMOC's deep overturning cell weakens (Fig. 20f), resulting in AABW reversal and its formation at shallower depths in the Pacific Sector of the Southern Ocean. The less dense, and likely warmer and fresher, AABW subsequently enters the Pacific, promoting clockwise convection. The subtropical North Atlantic overturning that contributes to AAIW formation in the Southern Hemisphere, maintains a similar structure, consistent with widespread surface warming (Fig. 18a) resulting from increased stratification in the warmer and fresher surface ocean (Fig. 19). The expansion of the clockwise cell in the North Pacific could also suggest an active PMOC during the LP with the formation of the North Pacific Deep Water (NPDW). However, as Figs. 20b and B.27 show, the upper PMOC cell exhibits no increasing trend during model runtime and its expansion can be attributed to the upper ocean salinization in the LP North Pacific (Fig. 18b). Therefore, our model does not indicate an active PMOC during the LP.

The Global Meridional Overturning Circulation (GMOC; Fig. 20a and d) exhibits a net weakening of deep water formation and export, particularly in the Southern Hemisphere. The PI simulation shows a strong anticlockwise cell representing the formation of AABW in the Southern Ocean, extending northward along the seafloor. During the LP, this AABW cell is significantly reduced, with the lower overturning streamfunction nearly disappearing. Taken together, the LP overturning structure reflects a more stratified ocean, with weaker AABW formation and a relatively stronger AMOC, consistent with large-scale changes in ocean circulation under Late Pliocene boundary conditions, indicated

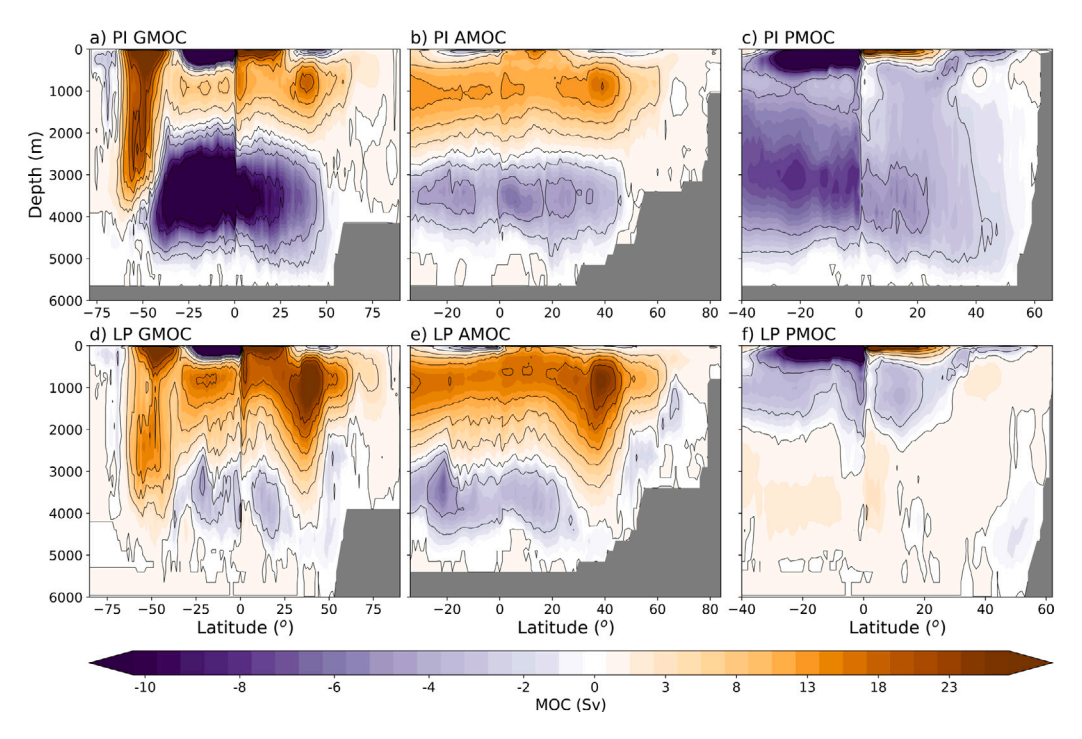


Fig. 20. Meridional Overturning Circulation (MOC) stream functions in different ocean domains (a, b, c) for the PI and (d, e, f) for the LP experiments. We show in (a, d) global MOC (GMOC) that is derived integrating over all ocean basins, (b, e) Atlantic MOC (AMOC) for the Atlantic Ocean only, (c, f) Pacific MOC (PMOC) for the Pacific Ocean only. Positive values (orange) indicate clockwise overturning cells, while negative values (purple) represent anticlockwise transport. (For interpretation of the references to color in this figure legend, the reader is referred to the web version of this article.)

by the PlioMIP2 model ensemble (Zhang et al., 2021b; Weiffenbach et al., 2023).

During model runtime, the PI GMOC maintains relative stability, with the AABW cell contributing approximately 18 Sv globally (Fig. 21a). A stagnant PMOC of about 2 Sv remaining secondary to the AMOC contribution to GMOC. The PMOC remains nearly absent during the LP simulation, corroborating the lack of deep water formation in the North Pacific. In LP simulation, surface freshening in the Pacific Ocean (Fig. 18b), and enhanced global upper-ocean stratification (Fig. 19) indicates inhibited development of the density gradients required for deep water formation in the North Pacific.

The overall strength of the global Antarctic Bottom Water (AABW) cell is notably reduced in LP (Fig. 21b), from 17.2 Sv in PI to 6 Sv, as the Pacific branch significantly weakens relative to the PI state (from 8.1 to 2.3 Sv in absolute values), while the Atlantic branch initially weakens (from 6.8 Sv in PI to 3.5 Sv in the first 50 years of LP) and then recovers towards the end of the simulation to about 6.4 Sv. This reduction likely reflects the widespread retreat of Antarctic sea-ice in both summer and winter (Fig. 17), but especially in the Pacific sector of the Southern Ocean, which limits brine rejection, ultimately suppressing bottom water formation. The resulting weakening of abyssal ventilation contributes to the ongoing deep ocean warming of about 5 °C, observed in the LP (Fig. 19), as heat becomes trapped in the poorly ventilated interior. Together, these overturning diagnostics reveal that the LP climate simulated in AWI-CM3 is characterized by a stronger AMOC (from 16.6 Sv to 25.2 Sv), a stagnant PMOC remaining near 1.3 Sy, and a substantially weakened AABW globally that is reversed in the Pacific. This reorganization results in a more hemispherically asymmetric overturning structure dominated by North Atlantic deep water formation, represented by the strong AMOC, and with a diminished role of the Southern Ocean, represented by the weaker global AABW. These changes reinforce broader climate patterns across the LP simulation, linking ocean circulation to sea-ice loss, albedo feedbacks, and regional salinity contrasts within the ocean-atmosphere system.

#### 4.3.3. Ocean meridional heat transport

To assess the impact of changes in large-scale ocean circulation on energy redistribution in major ocean basins, we analyze the average Meridional Ocean Heat Transport (OHT; Fig. 22). The top panel (Fig. 22a) shows total northward OHT in the PI and LP simulations for the global ocean, Atlantic, and Pacific basins. Zonal anomalies (LP minus PI) are presented to highlight shifts in the location and magnitude of poleward heat flux.

Across the tropics and temperate zones (approximately 60°S–60°N), the LP simulation exhibits a global reduction in southward heat transport and enhancement in northward heat transport. While southward heat transport is reduced in the Pacific and Atlantic basins, enhanced northward heat transport is primarily confined to the Atlantic basin. This pattern likely reflects a hemispheric energy imbalance resulting from salinization of the upper Atlantic Ocean driven by a strengthened AMOC (Figs. 20 and 21). Further investigation into the drivers of this strengthening is addressed in forthcoming publications. The Pacific basin displays similar anomalies to the Atlantic basin until 10°S. South of this latitude until 50°S, however, both exhibit opposite anomalies, with the Pacific (Atlantic) basin displaying reduced (increased) northward heat transport.

Between 30° to 40°N, the Pacific basin shows a slight increase in poleward heat transport that could suggest the development of an active PMOC in the LP. However, this increase is rather small and, together with our findings in Section 4.3.2, does not support an active PMOC. Additionally, an active PMOC in the Late Pliocene is a highly controversial feature, with limited supporting evidence from proxybased (Burls et al., 2017; Shankle et al., 2021; Ford et al., 2022; Fu and Fedorov, 2024) and modeling (Fu and Fedorov, 2024) studies. Conversely, global poleward heat transport in the Southern Hemisphere is enhanced south of 60°S in the LP, potentially indicating intensified Southern Ocean overturning or zonal asymmetries in eddy compensation. This enhancement correlates with extensive sea-ice formation in the Pacific sector of the Southern Ocean during the austral summer (Fig. 16b), driven by changes in Antarctic land-sea configuration (Fig. 5).

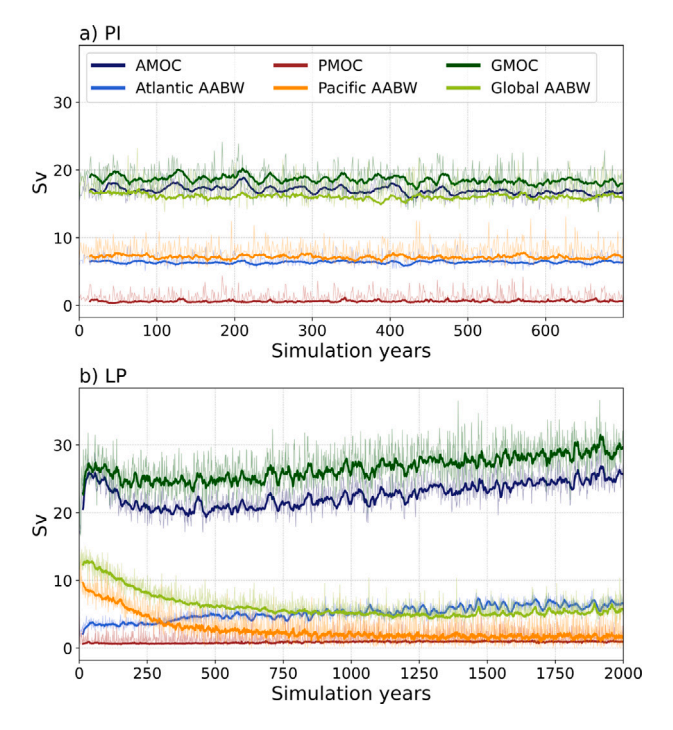


Fig. 21. Time evolution of the strength of the meridional overturning circulation (MOC) in the PI (a) and LP (b) simulations. The Atlantic Meridional Overturning Circulation (AMOC; blue), Pacific Meridional Overturning Circulation (PMOC; orange), and Global Mean Overturning Circulation (GMOC; green) are shown, alongside the contributions from Antarctic Bottom Water (AABW) formation in the Atlantic (purple), Pacific (red), and global ocean (light green). The MOC strengths are calculated with maximum strength of the upper overturning cell (from 500 m to 2000 m) calculated between 30° to 65°N, while AABW is calculated as the minimum strength of the lower overturning cell (from 2000 m to 6000 m) computed between 34°S and 35°N. (For interpretation of the references to color in this figure legend, the reader is referred to the web version of this article.)

These basin-scale differences emphasize the influence of basin geometry and surface buoyancy fluxes on regional ocean heat transport, and highlight the increased relevance of the Atlantic Ocean in providing interhemispheric and northward ocean heat transport in the LP.

#### 5. Summary and conclusions

We have presented here the first application of the AWI-CM3 coupled climate model to simulate the Late Pliocene climate under PlioMIP3 boundary conditions (LP simulation), with an extensive description of the methodology implemented. Additionally, we have illustrated various large-scale climate features in comparison to the Pre-Industrial (PI) reference state, including discussions that positions our findings in perspective with respect to the PlioMIP2 model ensemble and existing literature. Please note that a comprehensive comparison of our results with proxy records, as well as description of PlioMIP3 extension, optional and legacy experiments is beyond the scope of this study and will be addressed in forthcoming publications.

Our AWI-CM3 LP simulation features substantial polar warming, a restructured hydrological cycle, intensified monsoons, reduced meridional temperature gradients, extensive summer sea-ice loss, and an increased global mean surface temperature. Therefore, with AWI-CM3 we reproduce key features of the Marine Isotope Stage KM5c that closely align with proxy data compilations and other similar modeling studies (McClymont et al., 2020b, 2023a; Salzmann et al., 2008; Feng et al., 2022; Tierney et al., 2025; Haywood et al., 2020). Ocean and atmosphere exhibit strong coupling of heat, with pronounced atmospheric warming coinciding with amplified SSTs and generally leading

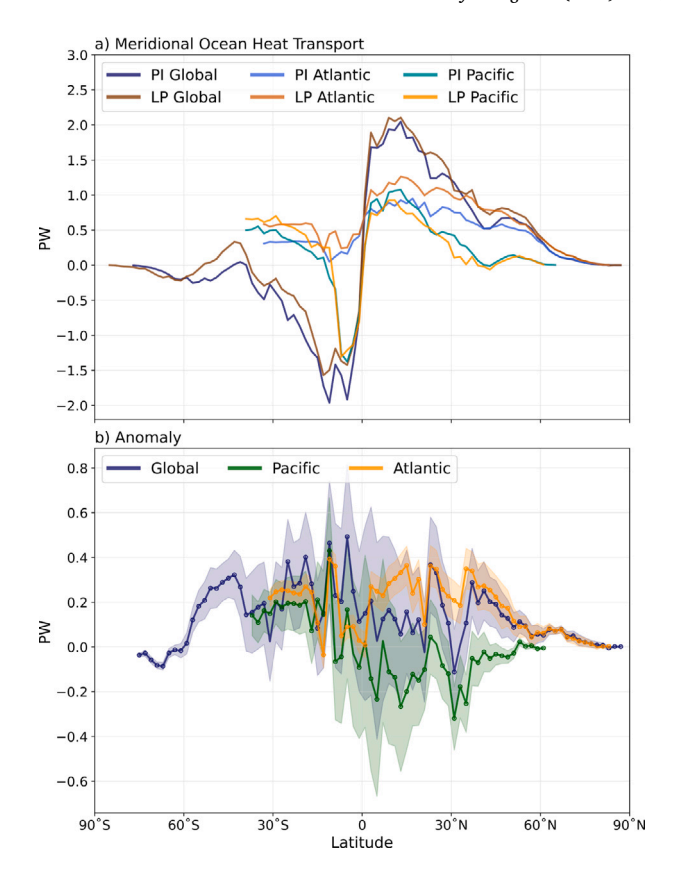


**Fig. 22.** Meridional ocean heat transport (OHT) in the PI and LP simulations for the global ocean, Atlantic Ocean, and Pacific Ocean. The top panel (a) shows the total northward OHT (in units of petawatts (PW);  $1PW = 10^{15}W$ ) as a function of latitude, while the bottom panel (b) shows the anomaly (LP minus PI). haded areas denote the interannual standard deviation over the final 200 simulation years. Circle markers indicate latitudes where anomalies are statistically significant at the 95% confidence level.

to various similarities in LP SST and SAT patterns. However, hydroclimate and salinity at the near surface induce heterogeneity in the overall climate response to LP forcing, as regions where warming in the ocean and atmosphere occur are not necessarily regions that become wetter and more saline (Figs. 12 and 18). Subtropical gyres and regions that are arid today, like the Sahel and Northeast Brazil, become warmer and drier, while high latitudes and the tropics experience both warmer and wetter conditions. Glacial-isostatic adjustments in Antarctica, resulting from reduced ice sheets, induce distinct atmospheric temperature and precipitation patterns in the polar Southern Hemisphere, with increased surface height of the ice sheet in central Antarctica inducing colder and drier conditions, contrasted by warmer and wetter conditions in adjacent areas (see Graphical Abstract). Conversely, warmer and wetter atmospheric conditions develop over vast parts of Antarctica, particularly where the AIS was reduced in the LP simulation with respect to PI.

We find a picture of generally warmer and fresher ocean surface. In particular the North Atlantic Ocean, Arctic Ocean marginal seas, north-western Pacific Ocean, and Atlantic and Indian Ocean sectors of the Southern Ocean show a LP SST pronounced anomaly. On the other hand, the North Atlantic, Arctic marginal seas (in particular Baffin Bay and Laptev Sea), and localized regions within the Atlantic and Indian sectors of the Southern Ocean show saltier upper ocean conditions, corroborated by the PlioMIP2 ensemble (Haywood et al., 2020) and by a recent data assimilation study (Tierney et al., 2025). The Pacific sector exhibits colder and fresher conditions within the Circumpolar Deep Water (CDW) outcrop region. Various enclosed or marginal seas,

including the Sea of Japan, the Yellow Sea, the Mediterranean Sea, the Red Sea, and the central Arctic Ocean, become fresher in the LP, a feature that appears in line with an overall enhanced hydrological cycle with increased continental runoff.

Simulated LP precipitation patterns reflect a global hydrological cycle reorganization driven by surface warming and polar amplification. Increased annual mean precipitation is observed in the tropics and mid-latitudes, with pronounced seasonal intensification during boreal summer. Monsoonal regions (South Asia, West Africa, and Central America) exhibit significant wet anomalies, indicative of amplified monsoon regimes, congruent with a wetter Pliocene and other warm climate analogs (Berntell et al., 2021; Han et al., 2021; Feng et al., 2022; Brierley et al., 2020; Otto-Bliesner et al., 2021; Ren et al., 2023; Sun et al., 2024), and supported by reconstructed wetland expansion and tropical forest distribution data (Salzmann et al., 2008). Additionally, increased high-latitude precipitation, particularly over Eurasia and coastal Antarctica, corresponds with reduced sea-ice and enhanced poleward heat transport. Hemispheric asymmetry is evident in tropical and subtropical regions, with the Southern Hemisphere exhibiting drier conditions, likely associated with a northward shift of the ITCZ that is consistent with findings by Pontes et al. (2020).

Our model shows substantial reductions in Arctic and Antarctic sea-ice in the LP due to the simulated surface warming (Figs. 15 and 16), leading to heavily reduced sea-ice concentration during summers in both hemispheres. Decreased surface albedo (Fig. 14) and altered Arctic and Antarctic continental outlines and ocean gateways (Fig. 5) contribute to high latitude amplified warming (Hill et al., 2014; Otto-Bliesner et al., 2017b), consistent with other PlioMIP2 models (Chandan and Peltier, 2018; Zheng et al., 2019; de Nooijer et al., 2020). Additionally, Antarctic sea-ice is primarily confined to the Pacific Sector, correlating with regional variations in atmospheric warming, precipitation, and Southern Ocean stratification (Weiffenbach et al., 2024).

An important question is after the degree of analogy between the Pliocene and future warm climates that arise from anthropogenic activity. One aspect of the research of paleoclimates is the idea that we can learn from past warm climates about potential climate patterns of the future. A key divergence between our simulation and typical results from future projections refers to the strength of the Atlantic Meridional Overturning Circulation (AMOC). In contrast to expected AMOC weakening under future global warming scenarios (Fox-Kemper et al., 2021), our LP simulation features a strengthened AMOC (Fig. 22e), aligning with PlioMIP2 models that employ similar paleogeographic boundary conditions in a quasi-equilibrium modeling framework (Weiffenbach et al., 2023; Zhang et al., 2021b). Intensification of the AMOC in simulation LP is, at least partly, attributed to increased salinity in the North Atlantic (Fig. 18b) resulting from the closure of the Bering Strait and Canadian Archipelago, restricting Arctic freshwater inflow (e.g., Otto-Bliesner et al., 2017b). The resulting dense North Atlantic surface waters promote deep convection and a more vigorous AMOC (Fig. 20e). Enhanced northward ocean heat transport in the Atlantic Ocean basin (Fig. 22), the maintenance of a deep winter mixed layer depth (Fig. B.26), and temporal evolution of overturning strength (Figs. 21 and B.27) further support this finding. However, in the context of AMOC, the latitudinal shift in the convection sites (Fig. B.26) align with the findings of multiple studies tackling warm climates (e.g., Lique and Thomas, 2018; Gou et al., 2024; Chafik and Rossby, 2019; Årthun et al., 2023), which further underscores the complexity of an analogy approach from Pliocene to future climate at least with regard to large-scale ocean circulation. Overall, the simulated strengthening of the AMOC, in contrast to its projected weakening under future global warming, highlights the pivotal role of tectonic boundary conditions, like the closure (opening) of Arctic (Antarctic) gateways, in shaping ocean circulation.

Conversely, our LP simulation indicates an inactive Pacific Meridional Overturning Circulation (PMOC), contrasting with some other modeling studies and reconstructions (Shankle et al., 2021; Ford et al., 2022; Fu and Fedorov, 2024; Burls et al., 2017), but consistent with the PlioMIP2 ensemble (Zhang et al., 2021b). The absence of an active Pacific Meridional Overturning Circulation (PMOC) further reduces global overturning complexity, emphasizing the dominant role of the Atlantic in the global surface heat distribution and in deep ocean ventilation during the Pliocene. Figs. 20 and B.27 corroborate strong AMOC and weak PMOC throughout the LP simulation. These factors likely contribute to increased ocean stratification, evidenced by temporal trends in deep ocean temperature and salinity (Fig. 19), indicating warming and freshening, and reduced vertical mixing.

Overall, while the Late Pliocene shares some climatic features with future warming scenarios, our findings caution against overly simplistic analogies. The distinct boundary conditions of the Pliocene climate system, particularly ocean gateway configurations and ice sheet extent, substantially alter ocean and atmospheric circulation and associated feedbacks and need to be further explored to assess degrees of climate analogy or rather analogous processes with respect to warm climates across timescales. However, the ocean's role in modulating heat transport in our LP simulation provides a robust background for evaluating Earth system sensitivity and long-term equilibrium responses to various forcings. As a logical next step, sensitivity experiments within the PlioMIP3 framework will be addressed and are essential to disentangle the relative roles of geographic, orbital, and atmospheric forcings in shaping Pliocene climate dynamics, thus mitigating data-model discrepancies, and improving the relevance of warm-period analogs for future climate projections.

#### CRediT authorship contribution statement

Fernanda DI Alzira Oliveira Matos: Writing - review & editing, Writing - original draft, Visualization, Validation, Software, Methodology, Investigation, Formal analysis, Data curation, Conceptualization. Christian Stepanek: Writing - review & editing, Writing - original draft, Supervision, Resources, Project administration, Methodology, Funding acquisition, Conceptualization. Sven Harig: Writing - review & editing, Software, Methodology. Jan Streffing: Writing - review & editing, Software, Methodology. Qiong Zhang: Writing - review & editing, Supervision, Resources, Methodology. Zhenqian Wang: Writing review & editing, Methodology. Katherine Power: Writing - review & editing, Methodology. Tido Semmler: Writing - review & editing, Supervision. Dmitry Sidorenko: Writing – review & editing, Software. Patrick Scholz: Writing - review & editing, Software. Sergey Danilov: Writing - review & editing, Software. Paul Gravis: Writing - review & editing. Gerrit Lohmann: Writing - review & editing, Supervision, Resources, Conceptualization.

#### **Declaration of competing interest**

The authors declare the following financial interests/personal relationships which may be considered as potential competing interests: Fernanda DI Alzira Oliveira Matos reports financial support and travel were provided by German Academic Exchange Service. If there are other authors, they declare that they have no known competing financial interests or personal relationships that couldhave appeared to influence the work reported in this paper.

#### Acknowledgments

This work was supported by the INSPIRES (International Science Program for Integrative Research in Earth Systems), at the Alfred Wegener Institute, Helmholtz Centre for Polar and Marine Research and the DAAD, German (German Exchange Service) during the research stay abroad of F.D.A.O.M. at Stockholm University to develop the methodology for adapting AWI-CM3 to paleogeographies. This work is also supported by the European Research Council grant "i2B" (Into

Table A.6

Overview on model variables in OpenIFS and FESOM2.5 and the choice of method/treatment to adapt them for the LP simulation.

Method	OpenIFS variables in Gaussian grid	OpenIFS variables in spectral grid	FESOM2.5 variables	
Anomaly Land-sea mask, Lake cover		Geopotential (land elevation)	Bathymetry	
Replacement	Snow depth (ice sheet)	-	-	
Lookup table	Leaf Area Index (high and low vegetation), Soil type, Type of Vegetation (high and low vegetation), Vegetation cover (high and low vegetation), Volumetric soil water layer 1 [1-4]	-	-	
CALNORO	Angle of subgridscale orography, Anisotropy of subgridscale orography, Slope of subgridscale orography, Standard deviation of orography	-	-	
DWA	Albedo, Charnock Parameter, Ice temperature layer [1-4], Lake depth, Lake ice depth, Lake mix-layer depth, Lake mix-layer temperature, Lake shape factor, Near IR albedo for diffuse radiation, Sea ice fraction, Sea surface temperature, Skin reservoir, Skin temperature, Soil temperature level [1-4], Snow albedo, Snow density, Standard deviation of filtered subgridscale orography, Temperature of snow layer, UV visible albedo for direct radiation, UV visible albedo for diffuse radiation	-	-	
No change	Logarithm of surface roughness length for heat, Surface roughness	Divergence, Logarithm of surface pressure, Temperature, Vorticity	-	

Table A.7

Translation of the OpenIFS soil texture and volumetric soil water layer fields (in units of m<sup>3</sup>m<sup>-3</sup>; volume of water to the volume of soil).

, .				
Translated soil types	Volumetric soil water layer 1 (0 – 7 cm)	Volumetric soil water layer 2 (7 – 28 cm)	Volumetric soil water layer 3 (28 – 100 cm)	Volumetric soil water layer 4 (100 – 289 cm)
Coarse	0.210	0.212	0.208	0.188
Medium	0.283	0.279	0.270	0.300
Medium Fine	0.373	0.374	0.375	0.399
Fine	0.209	0.248	0.262	0.255

the Blue; grant no. 101118519), funded by the European Union. Views and opinions expressed are however those of the author(s) only and do not necessarily reflect those of the European Union or the European Research Council Executive Agency. Neither the European Union nor the granting authority can be held responsible for them. The authors would also like to acknowledge the Jülich Supercomputing Centre (JSC) and the German Climate Computing Centre (DKRZ) for providing computing time on the supercomputers JUWELS and LEVANTE, respectively. The Python packages pyfesom2 (https://github.com/FESOM/pyfesom2, last access: 10 July 2025) and tripyview (https://github.com/FESOM/tripyview, last access: 10 July 2025), as well as CDO version 2.4.1(Schulzweida, 2023, last access: 10 July 2025) were utilized for post-processing and plotting of the data. Finally, we thank the reviewers for their constructive feedback and comments that have greatly increased the quality of our manuscript.

#### Appendix A. OpenIFS initial and boundary conditions

See Figs. A.23-A.25 and Tables A.6 and A.7.

### Appendix B. MOC supporting figures

See Figs. B.26-B.28.

#### Data availability

For data access requests and analyses codes, please refer initially to F.D.A.O.M. (fernanda.matos@awi.de). However, the model output will be later uploaded to the PlioMIP3 data repository.

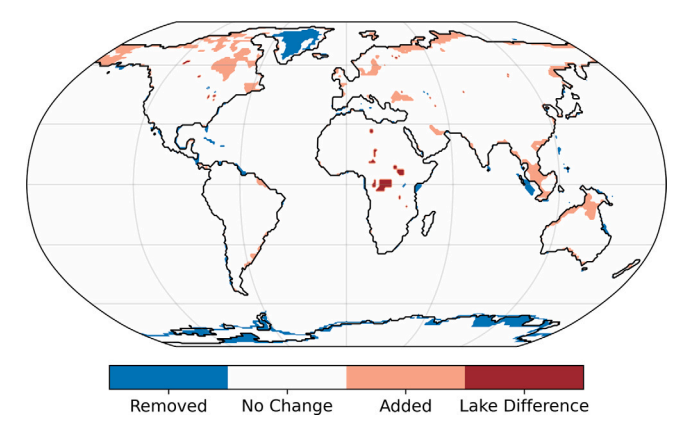


Fig. A.23. Differences in OpenIFS land—sea and lake masks between the LP and PI boundary conditions after adjustments and corrections. Colored areas indicate regions that underwent a transition in surface type between LP and PI: light red marked regions changed from ocean to land from PI to LP (e.g., exposed continental shelves), dark red represent regions of change in lake cover, and blue tones indicate areas that became submerged or converted from ice-sheets into land from PI to LP. (For interpretation of the references to color in this figure legend, the reader is referred to the web version of this article.)

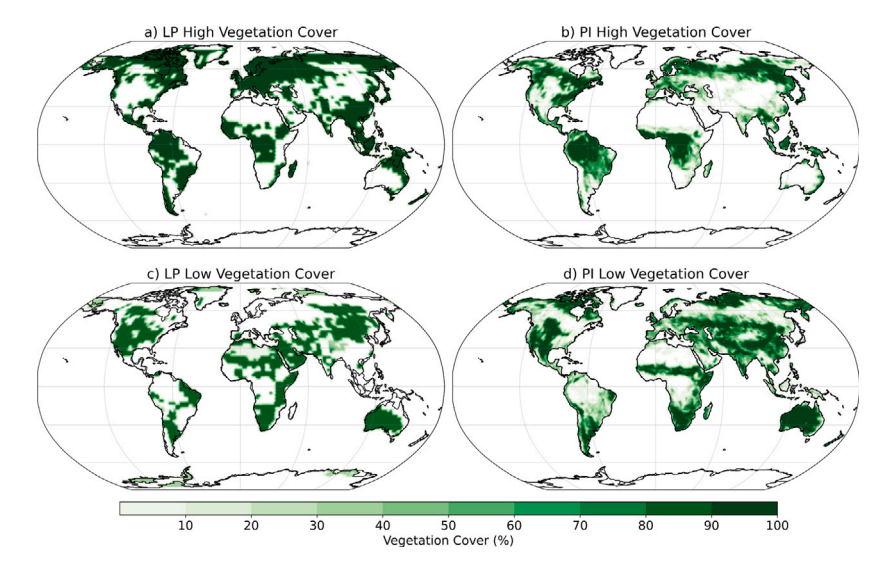


Fig. A.24. Prescribed vegetation cover for the PlioMIP3 LP and PI experiments with AWI-CM3. (a, b) High vegetation and (b, c) low vegetation. (a, c) LP and (b, d) PI.

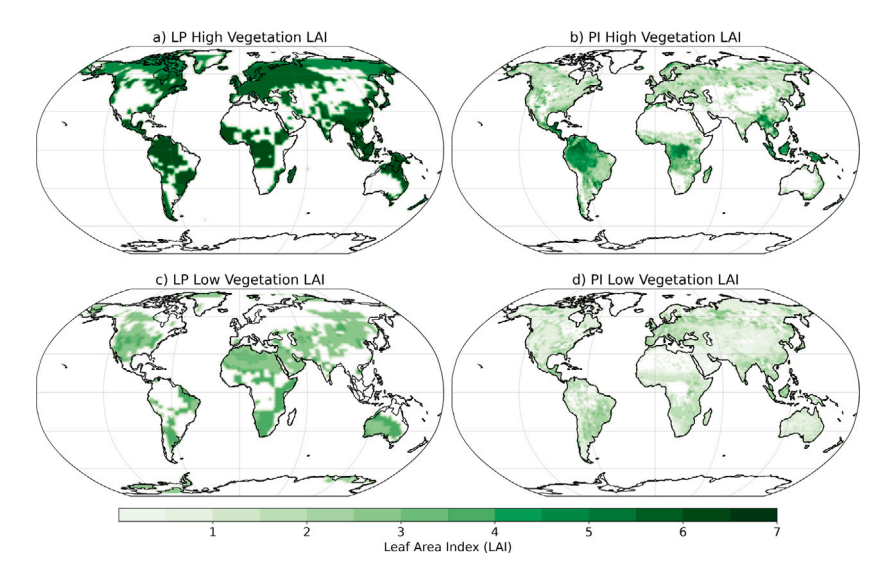


Fig. A.25. Prescribed Leaf Area Index (LAI) for the PlioMIP3 LP and PI experiments with AWI-CM3. (a, b) High vegetation and (b, c) low vegetation. (a, c) LP and (b, d) PI.

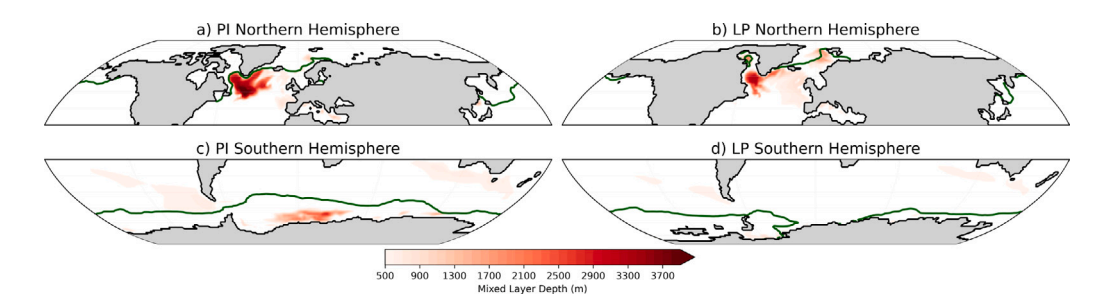


Fig. B.26. Mixed Layer Depth over 500 m in (a, c) the PI and (b, d) LP for the (a, b) Northern Hemisphere and (c, d) Southern Hemisphere. Superimposed in green is the sea-ice edge corresponding to the 15% sea-ice concentration contour. (For interpretation of the references to color in this figure legend, the reader is referred to the web version of this article.)

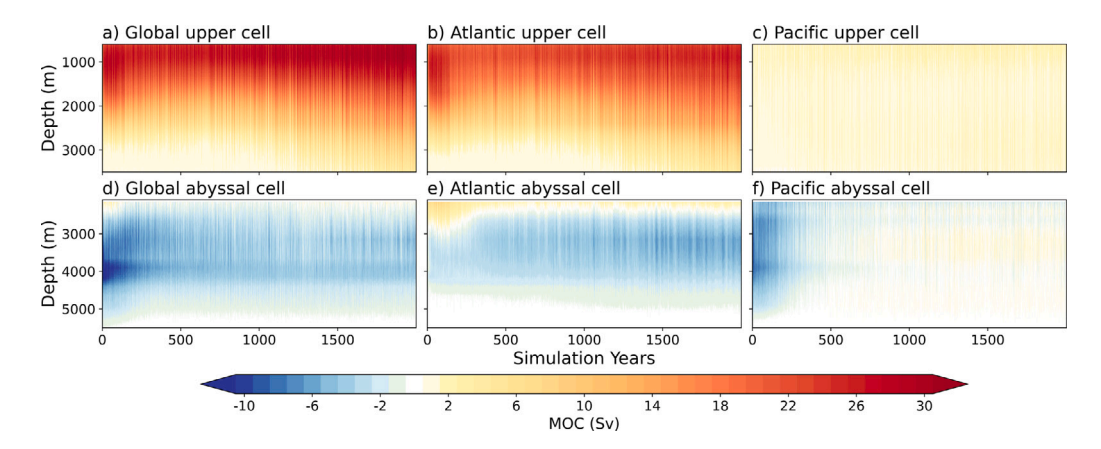
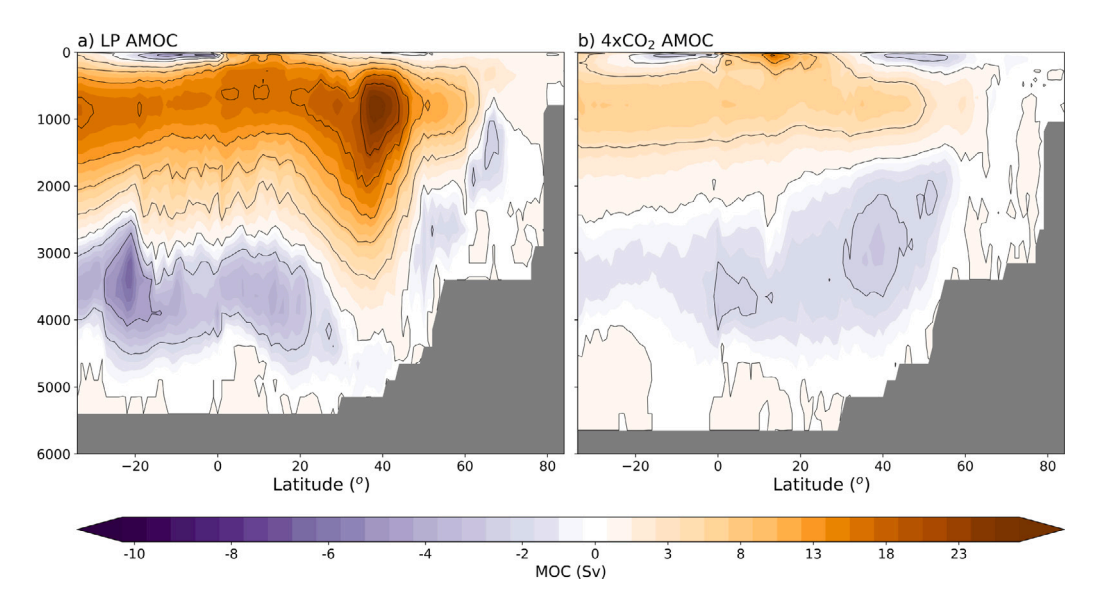


Fig. B.27. Hovmöller diagrams of the Meridional Overturning Circulation (MOC) streamfunction (Sv) as a function of latitude and model year for the Global (a, d), Atlantic (b, e), and Pacific (c, f) sectors. The upper panels display the maximum strength of the upper overturning cell (clockwise, in red) calculated between 30° to 65°N, while the lower panels show the minimum strength of the lower overturning cell (anticlockwise, in blue) computed between 34°S and 35°N. (For interpretation of the references to color in this figure legend, the reader is referred to the web version of this article.)



**Fig. B.28.** Atlantic Meridional Overturning Circulation (AMOC) stream functions (a) LP and (b) *4xCO*<sub>2</sub> experiments. Positive values (orange) indicate clockwise overturning cells, while negative values (purple) represent anticlockwise transport. (For interpretation of the references to color in this figure legend, the reader is referred to the web version of this article.)

#### References

Årthun, M., Asbjørnsen, H., Chafik, L., Johnson, H.L., Våge, K., 2023. Future strengthening of the Nordic Seas overturning circulation. Nat. Commun. 14 (1), 2065. http://dx.doi.org/10.1038/s41467-023-37846-6.

Baines, P.G., Palmer, T.N., 1990. Rationale for a new physically based parametrization of subgrid-scale orographic effects. ECMWF Tech. Memo. 169, 11. http://dx.doi. org/10.21957/h4h36b3u.

Baker, J.A., Bell, M.J., Jackson, L.C., Vallis, G.K., Watson, A.J., Wood, R.A., 2025. Continued Atlantic overturning circulation even under climate extremes. Nature 638 (8052), 987–994. http://dx.doi.org/10.1038/s41586-024-08544-0.

Balsamo, G., Beljaars, A., Scipal, K., Viterbo, P., Hurk, B.v.d., Hirschi, M., Betts, A.K., 2009. A revised hydrology for the ECMWF model: Verification from field site to terrestrial water storage and impact in the integrated forecast system. J. Hydrometeorol. 10 (3), 623–643. http://dx.doi.org/10.1175/2008JHM1068.1.

Barbi, D., Wieters, N., Gierz, P., Andrés-Martínez, M., Ural, D., Chegini, F., Khosravi, S., Cristini, L., 2021. ESM-Tools version 5.0: a modular infrastructure for stand-alone and coupled Earth system modelling (ESM). Geosci. Model. Dev. 14 (6), 4051–4067. http://dx.doi.org/10.5194/gmd-14-4051-2021.

Berntell, E., Zhang, Q., Li, Q., Haywood, A.M., Tindall, J.C., Hunter, S.J., Zhang, Z., Li, X., Guo, C., Nisancioglu, K.H., Stepanek, C., Lohmann, G., Sohl, L.E., Chandler, M.A., Tan, N., Contoux, C., Ramstein, G., Baatsen, M.L.J., von der Heydt, A.S., Chandan, D., Peltier, W.R., Abe-Ouchi, A., Chan, W.-L., Kamae, Y., Williams, C.J.R., Lunt, D.J., Feng, R., Otto-Bliesner, B.L., Brady, E.C., 2021. Mid-Pliocene West African Monsoon rainfall as simulated in the PlioMIP2 ensemble. Clim. the Past 17 (4), 1777–1794. http://dx.doi.org/10.5194/cp-17-1777-2021.

Brierley, C.M., Zhao, A., Harrison, S.P., Braconnot, P., Williams, C.J.R., Thornalley, D.J.R., Shi, X., Peterschmitt, J.-Y., Ohgaito, R., Kaufman, D.S., Kageyama, M., Hargreaves, J.C., Erb, M.P., Emile-Geay, J., D'Agostino, R., Chandan, D., Carré, M., Bartlein, P.J., Zheng, W., Zhang, Z., Zhang, Q., Yang, H., Volodin, E.M., Tomas, R.A., Routson, C., Peltier, W.R., Otto-Bliesner, B., Morozova, P.A., McKay, N.P., Lohmann, G., Legrande, A.N., Guo, C., Cao, J., Brady, E., Annan, J.D., Abe-Ouchi, A., 2020. Large-scale features and evaluation of the PMIP4-CMIP6 midholocene simulations. Clim. the Past 16 (5), 1847–1872. http://dx.doi.org/10.5194/cp-16-1847-2020.

Broecker, W.S., 1991. The great ocean conveyor. Oceanography 4 (2), 79–89. http://dx.doi.org/10.5670/oceanog.1991.07.

Buizza, R., Bechtold, P., Bonavita, M., Bormann, N., Bozzo, A., Haiden, T., Hogan, R., Hólm, E., Radnoti, G., Richardson, D., Sleigh, M., 2017. IFS cycle 43r3 brings model and assimilation updates. ECMWF Newsl. 152, 18–22. http://dx.doi.org/10.21957/ 76t4e1.

Burke, K.D., Williams, J.W., Chandler, M.A., Haywood, A.M., Lunt, D.J., Otto-Bliesner, B.L., 2018. Pliocene and Eocene provide best analogs for near-future climates. Proc. Natl. Acad. Sci. 115 (52), 13288–13293. http://dx.doi.org/10.1073/pnas.1809600115.

Burls, N.J., Fedorov, A.V., Sigman, D.M., Jaccard, S.L., Tiedemann, R., Haug, G.H., 2017. Active Pacific meridional overturning circulation (PMOC) during the warm pliocene. Sci. Adv. 3 (9), e1700156. http://dx.doi.org/10.1126/sciadv.1700156.

- Burton, L.E., Haywood, A.M., Tindall, J.C., Dolan, A.M., Hill, D.J., McClymont, E.L., Ho, S.L., Ford, H.L., 2024. The role of atmospheric CO<sub>2</sub> in controlling sea surface temperature change during the Pliocene. Clim. the Past 20 (5), 1177–1194. http: //dx.doi.org/10.5194/cp-20-1177-2024.
- Burton, L.E., Oldeman, A.M., Haywood, A.M., Tindall, J.C., Dolan, A.M., Hill, D.J., von der Heydt, A., Baatsen, M.L.J., 2025. An assessment of the Pliocene as an analogue for our warmer future. Glob. Planet. Change 252, 104860. http://dx.doi.org/10.1016/j.gloplacha.2025.104860.
- Chafik, L., Rossby, T., 2019. Volume, heat, and freshwater divergences in the subpolar North Atlantic suggest the Nordic Seas as key to the state of the meridional overturning circulation. Geophys. Res. Lett. 46 (9), 4799–4808. http://dx.doi.org/10.1029/2019GL082110.
- Chandan, D., Peltier, W.R., 2018. On the mechanisms of warming the mid-Pliocene and the inference of a hierarchy of climate sensitivities with relevance to the understanding of climate futures. Clim. the Past 14 (6), 825–856. http://dx.doi.org/10.5194/cp-14-825-2018.
- Craig, A., Valcke, S., Coquart, L., 2017. Development and performance of a new version of the OASIS coupler, OASIS3-MCT\_3.0. Geosci. Model. Dev. 10 (9), 3297–3308. http://dx.doi.org/10.5194/gmd-10-3297-2017.
- Danilov, S., Sidorenko, D., Wang, Q., Jung, T., 2017. The finite-volume sea ice-ocean model (FESOM2). Geosci. Model. Dev. 10 (2), 765–789. http://dx.doi.org/10.5194/ gmd-10-765-2017.
- Danilov, S., Wang, Q., Timmermann, R., Iakovlev, N., Sidorenko, D., Kimmritz, M., Jung, T., Schröter, J., 2015. Finite-element sea ice model (FESIM), version 2. Geosci. Model. Dev. 8 (6), 1747–1761. http://dx.doi.org/10.5194/gmd-8-1747-2015.
- de Nooijer, W., Zhang, Q., Li, Q., Zhang, Q., Li, X., Zhang, Z., Guo, C., Nisan-cioglu, K.H., Haywood, A.M., Tindall, J.C., Hunter, S.J., Dowsett, H.J., Stepanek, C., Lohmann, G., Otto-Bliesner, B.L., Feng, R., Sohl, L.E., Chandler, M.A., Tan, N., Contoux, C., Ramstein, G., Baatsen, M.L.J., von der Heydt, A.S., Chandan, D., Peltier, W.R., Abe-Ouchi, A., Chan, W.-L., Kamae, Y., Brierley, C.M., 2020. Evaluation of Arctic warming in mid-Pliocene climate simulations. Clim. the Past 16 (6), 2325–2341. http://dx.doi.org/10.5194/cp-16-2325-2020.
- Dowsett, H., Dolan, A., Rowley, D., Moucha, R., Forte, A.M., Mitrovica, J.X., Pound, M., Salzmann, U., Robinson, M., Chandler, M., Foley, K., Haywood, A., 2016. The PRISM4 (mid-Piacenzian) paleoenvironmental reconstruction. Clim. the Past 12 (7), 1519–1538.
- Dowsett, H.J., Foley, K.M., Stoll, D.K., Chandler, M.A., Sohl, L.E., Bentsen, M., Otto-Bliesner, B.L., Bragg, F.J., Chan, W.-L., Contoux, C., Dolan, A.M., Haywood, A.M., Jonas, J.A., Jost, A., Kamae, Y., Lohmann, G., Lunt, D.J., Nisancioglu, K.H., Abe-Ouchi, A., Ramstein, G., Riesselman, C.R., Robinson, M.M., Rosenbloom, N.A., Salzmann, U., Stepanek, C., Strother, S.L., Ueda, H., Yan, Q., Zhang, Z., 2013. Sea surface temperature of the mid-Piacenzian Ocean: A data-model comparison. Sci. Rep. 3 (1), 2013. http://dx.doi.org/10.1038/srep02013.
- Dowsett, H.J., Robinson, M.M., Foley, K.M., Hunter, S.J., Dolan, A.M., Tindall, J.C., 2023. Early Pliocene (Zanclean) stratigraphic framework for PRISM5/PlioMIP3 time slices. Stratigraphy 20 (3), 225–231. http://dx.doi.org/10.29041/strat.20.3.02.
- Dowsett, H.J., Robinson, M.M., Haywood, A.M., Salzmann, U., Hill, D., Sohl, L., Chandler, M., Williams, M., Foley, K., Stoll, D.K., 2010. The PRISM3D paleoenvironmental reconstruction. Stratigraphy 7, 123–139. http://dx.doi.org/10.29041/ strat.07.2.03.
- ECMWF, 2017a. IFS Documentation CY43R3 Part I : Observations. pp. 1–123. http://dx.doi.org/10.21957/7z1cf0t3c, ECMWF, chapter 1.
- ECMWF, 2017b. IFS Documentation CY43R3 Part III: Dynamics and numerical procedures. pp. 1–170. http://dx.doi.org/10.21957/8l7miod5m, ECMWF, chapter
- ECMWF, 2017c. IFS Documentation CY43R3 Part IV: Physical processes. pp. 1–223. http://dx.doi.org/10.21957/efyk72kl, ECMWF, chapter 4.
- ECMWF, 2017d. IFS Documentation CY43R3 Part VI: Technical and computational procedures. pp. 1–198. http://dx.doi.org/10.21957/nrwhwmukh, ECMWF, chapter
- ECMWF, 2017e. IFS documentation CY43r3 part VII: ECMWF wave model. ECMWF, pp. 1–87. http://dx.doi.org/10.21957/mxz9z1gb,
- Eyring, V., Bony, S., Meehl, G.A., Senior, C.A., Stevens, B., Stouffer, R.J., Taylor, K.E., 2016. Overview of the coupled model intercomparison project phase 6 (CMIP6) experimental design and organization. Geosci. Model. Dev. 9 (5), 1937–1958. http://dx.doi.org/10.5194/gmd-9-1937-2016.
- Feng, R., Bhattacharya, T., Otto-Bliesner, B.L., Brady, E.C., Haywood, A.M., Tindall, J.C., Hunter, S.J., Abe-Ouchi, A., Chan, W.-L., Kageyama, M., Contoux, C., Guo, C., Li, X., Lohmann, G., Stepanek, C., Tan, N., Zhang, Q., Zhang, Z., Han, Z., Williams, C.J.R., Lunt, D.J., Dowsett, H.J., Chandan, D., Peltier, W.R., 2022. Past terrestrial hydroclimate sensitivity controlled by earth system feedbacks. Nat. Commun. 13 (1), 1306. http://dx.doi.org/10.1038/s41467-022-28814-7.
- Foley, K.M., Dowsett, H., 2019. Community Sourced Mid-Piacenzian Sea Surface Temperature (SST) Data. U.S. Geological Survey, http://dx.doi.org/10.5066/ P9YP3DTV.
- Ford, H.L., Burls, N.J., Jacobs, P., Jahn, A., Caballero-Gill, R.P., Hodell, D.A., Fedorov, A.V., 2022. Sustained mid-pliocene warmth led to deep water formation in the North Pacific. Nat. Geosci. 15, 658–663. http://dx.doi.org/10.1038/s41561-022-00978-3.

- Fox-Kemper, B., Hewitt, H., Xiao, C., Aðalgeirsdóttir, G., Drijfhout, S., Edwards, T., Golledge, N., Hemer, M., Kopp, R., Krinner, G., Mix, A., Notz, D., Nowicki, S., Nurhati, I., Ruiz, L., Sallée, J.-B., Slangen, A., Yu, Y., 2021. Ocean, cryosphere and sea level change. In: Masson-Delmotte, V., Zhai, P., Pirani, A., Connors, S., Péan, C., Berger, S., Caud, N., Chen, Y., Goldfarb, L., Gomis, M., Huang, M., Leitzell, K., Lonnoy, E., Matthews, J., Maycock, T., Waterfield, T., Yelekçi, O., Yu, R., Zhou, B. (Eds.), Climate Change 2021: The Physical Science Basis. Contribution of Working Group I to the Sixth Assessment Report of the Intergovernmental Panel on Climate Change. Cambridge University Press, Cambridge, United Kingdom and New York, NY, USA, pp. 1211–1362. http://dx.doi.org/10.1017/9781009157896.011.
- Fu, M., Fedorov, A.V., 2024. Impacts of an active Pacific meridional overturning circulation on the pliocene climate and hydrological cycle. Earth Planet. Sci. Lett. 642, 118878. http://dx.doi.org/10.1016/j.epsl.2024.118878.
- Gent, P.R., McWilliams, J.C., 1990. Isopycnal mixing in ocean circulation models. J. Phys. Oceanogr. 20, 150–155. http://dx.doi.org/10.1175/1520-0485(1990) 020<0150:IMIOCM>2.0.CO;2.
- Gou, R., Wang, Y., Xiao, K., Wu, L., 2024. A plausible emergence of new convection sites in the Arctic Ocean in a warming climate. Environ. Res. Lett. 19 (3), 031001. http://dx.doi.org/10.1088/1748-9326/ad2237.
- Gregory, J., Ingram, W., Palmer, M., Jones, G., Stott, P., Thorpe, R., Lowe, J., Johns, T., Williams, K., 2004. A new method for diagnosing radiative forcing and climate sensitivity. Geophys. Res. Lett. 31, L03205. http://dx.doi.org/10.1029/2003GI.018747
- Han, Z., Zhang, Q., Li, Q., Feng, R., Haywood, A.M., Tindall, J.C., Hunter, S.J., Otto-Bliesner, B.L., Brady, E.C., Rosenbloom, N., Zhang, Z., Li, X., Guo, C., Nisancioglu, K.H., Stepanek, C., Lohmann, G., Sohl, L.E., Chandler, M.A., Tan, N., Ramstein, G., Baatsen, M.L.J., von der Heydt, A.S., Chandan, D., Peltier, W.R., Williams, C.J.R., Lunt, D.J., Cheng, J., Wen, Q., Burls, N.J., 2021. Evaluating the large-scale hydrological cycle response within the Pliocene Model Intercomparison Project Phase 2 (PlioMIP2) ensemble. Clim. the Past 17 (6), 2537–2558. http://dx.doi.org/10.5194/cp-17-2537-2021.
- Haywood, A.M., Dolan, A.M., Pickering, S.J., Dowsett, H.J., McClymont, E.L., Prescott, C.L., Salzmann, U., Hill, D.J., Hunter, S.J., Lunt, D.J., Pope, J.O., Valdes, P.J., 2013. On the identification of a Pliocene time slice for data-model comparison. Philos. Trans. R. Soc. A: Math. Phys. Eng. Sci. 371 (2001), 20120515. http://dx.doi.org/10.1098/rsta.2012.0515.
- Haywood, A.M., Dowsett, H.J., Dolan, A.M., Rowley, D., Abe-Ouchi, A., Otto-Bliesner, B., Chandler, M.A., Hunter, S.J., Lunt, D.J., Pound, M., Salzmann, U., 2016. The Pliocene Model Intercomparison Project (PlioMIP) Phase 2: scientific objectives and experimental design. Clim. the Past 12 (3), 663–675. http://dx.doi.org/10.5194/cp-12-663-2016.
- Haywood, A.M., Dowsett, H.J., Otto-Bliesner, B., Chandler, M.A., Dolan, A.M., Hill, D.J., Lunt, D.J., Robinson, M.M., Rosenbloom, N., Salzmann, U., Sohl, L.E., 2010. Pliocene Model Intercomparison Project (PlioMIP): experimental design and boundary conditions (Experiment 1). Geosci. Model. Dev. 3, 227–242. http://dx.doi.org/ 10.5194/gmd-3-227-2010.
- Haywood, A.M., Dowsett, H.J., Robinson, M.M., Stoll, D.K., Dolan, A.M., Lunt, D.J., Otto-Bliesner, B., Chandler, M.A., 2011. Pliocene Model Intercomparison Project (PlioMIP): experimental design and boundary conditions (Experiment 2). Geosci. Model. Dev. 4 (3), 571–577. http://dx.doi.org/10.5194/gmd-4-571-2011.
- Haywood, A.M., Dowsett, H.J., Valdes, P.J., Lunt, D.J., Francis, J.E., Sellwood, B.W., 2008. Introduction. Pliocene climate, processes and problems. Philos. Trans. R. Soc. A: Math. Phys. Eng. Sci. 367 (1886), 3–17. http://dx.doi.org/10.1098/rsta.2008. 0205.
- Haywood, A.M., Tindall, J.C., Burton, L.E., Chandler, M.A., Dolan, A.M., Dowsett, H.J., Feng, R., Fletcher, T.L., Foley, K.M., Hill, D.J., Hunter, S.J., Otto-Bliesner, B.L., Lunt, D.J., Robinson, M.M., Salzmann, U., 2024. Pliocene Model Intercomparison Project Phase 3 (PlioMIP3) - Science plan and experimental design. Glob. Planet. Change 232, 104316. http://dx.doi.org/10.1016/j.gloplacha.2023.104316.
- Haywood, A.M., Tindall, J.C., Dowsett, H.J., Dolan, A.M., Foley, K.M., Hunter, S.J., Hill, D.J., Chan, W.-L., Abe-Ouchi, A., Stepanek, C., Lohmann, G., Chandan, D., Peltier, W.R., Tan, N., Contoux, C., Ramstein, G., Li, X., Zhang, Z., Guo, C., Nisancioglu, K.H., Zhang, Q., Li, Q., Kamae, Y., Chandler, M.A., Sohl, L.E., Otto-Bliesner, B.L., Feng, R., Brady, E.C., von der Heydt, A.S., Baatsen, M.L.J., Lunt, D.J., 2020. The Pliocene Model Intercomparison Project Phase 2: large-scale climate features and climate sensitivity. Clim. the Past 16 (6), 2095–2123. http://dx.doi.org/10.5194/cp-16-2095-2020.
- Haywood, A.M., Valdes, P.J., Aze, T., Barlow, N., Burke, A., Dolan, A.M., von der Heydt, A.S., Hill, D.J., Jamieson, S.S.R., Otto-Bliesner, B.L., Salzmann, U., Saupe, E., Voss, J., 2019. What can palaeoclimate modelling do for you? Earth Syst. Environ. 3, 1–18. http://dx.doi.org/10.1007/s41748-019-00093-1.
- Hill, D.J., Haywood, A.M., Lunt, D.J., Hunter, S.J., Bragg, F.J., Contoux, C., Stepanek, C., Sohl, L., Rosenbloom, N.A., Chan, W.-L., Kamae, Y., Zhang, Z., Abe-Ouchi, A., Chandler, M.A., Jost, A., Lohmann, G., Otto-Bliesner, B.L., Ramstein, G., Ueda, H., 2014. Evaluating the dominant components of warming in Pliocene climate simulations. Clim. the Past 10 (1), 79–90. http://dx.doi.org/10.5194/cp-10-79-2014.
- Jackson, L.C., Alastrué de Asenjo, E., Bellomo, K., Danabasoglu, G., Haak, H., Hu, A., Jungclaus, J., Lee, W., Meccia, V.L., Saenko, O., Shao, A., Swingedouw, D., 2023. Understanding AMOC stability: the North Atlantic Hosing Model Intercomparison

- Project. Geosci. Model. Dev. 16 (7), 1975–1995. http://dx.doi.org/10.5194/gmd-16-1975-2023.
- Jackson, L.C., Wood, R.A., 2018. Timescales of AMOC decline in response to fresh water forcing. Clim. Dyn. 51, 1333–1350. http://dx.doi.org/10.1007/s00382-017-3957-6.
- Kageyama, M., Braconnot, P., Harrison, S.P., Haywood, A.M., Jungclaus, J.H., Otto-Bliesner, B.L., Peterschmitt, J.-Y., Abe-Ouchi, A., Albani, S., Bartlein, P.J., Brierley, C., Crucifix, M., Dolan, A., Fernandez-Donado, L., Fischer, H., Hopcroft, P.O., Ivanovic, R.F., Lambert, F., Lunt, D.J., Mahowald, N.M., Peltier, W.R., Phipps, S.J., Roche, D.M., Schmidt, G.A., Tarasov, L., Valdes, P.J., Zhang, Q., Zhou, T., 2018. The PMIP4 contribution to CMIP6 Part 1: Overview and over-arching analysis plan. Geosci. Model. Dev. 11 (3), 1033–1057. http://dx.doi.org/10.5194/gmd-11-1033-2018.
- Koenig, S.J., Dolan, A.M., de Boer, B., Stone, E.J., Hill, D.J., DeConto, R.M., Abe-Ouchi, A., Lunt, D.J., Pollard, D., Quiquet, A., Saito, F., Savage, J., van de Wal, R., 2015. Ice sheet model dependency of the simulated Greenland Ice Sheet in the mid-Pliocene. Clim. the Past 11 (3), 369–381. http://dx.doi.org/10.5194/cp-11-369-2015.
- Koldunov, N.V., Aizinger, V., Rakowsky, N., Scholz, P., Sidorenko, D., Danilov, S., Jung, T., 2019. Scalability and some optimization of the finite-volume sea iceocean model, version 2.0 (FESOM2). Geosci. Model. Dev. 12 (9), 3991–4012. http://dx.doi.org/10.5194/gmd-12-3991-2019.
- Komen, G.J., Cavaleri, L., Donelan, M., Hasselmann, K., Hasselmann, S., Janssen, P.A.E.M., 1994. Dynamics and Modelling of Ocean Waves. Cambridge University Press, Cambridge, http://dx.doi.org/10.1017/CBO9780511628955.
- Large, W.G., Yeager, S.G., 2009. The global climatology of an interannually varying air-sea flux data set. Clim. Dyn. 33, 341–364. http://dx.doi.org/10.1007/s00382-008-0441-3.
- Lique, C., Thomas, M.D., 2018. Latitudinal shift of the Atlantic Meridional Overturning Circulation source regions under a warming climate. Nat. Clim. Chang. 8, 1013–1020. http://dx.doi.org/10.1038/s41558-018-0316-5.
- Lohmann, G., Pfeiffer, M., Laepple, T., Leduc, G., Kim, J.-H., 2013. A model-data comparison of the Holocene global sea surface temperature evolution. Clim. the Past 9, 1807–1839. http://dx.doi.org/10.5194/cp-9-1807-2013.
- Lott, F., 1999. Alleviation of stationary biases in a GCM through a mountain drag parameterization scheme and a simple representation of mountain lift forces. Mon. Weather Rev. 127, 788–801. http://dx.doi.org/10.1175/1520-0493(1999) 127<0788;AOSBIA>2.0.CO:2.
- Lott, F., Miller, M.J., 2013. A new subgrid-scale orographic drag parametrization: Its formulation and testing. Q. J. R. Meteorol. Soc. 123, 101–127. http://dx.doi.org/10.1002/qj.49712353704.
- Max, L., Nürnberg, D., Chiessi, C.M., Lenz, M.M., Mulitza, S., 2022. Subsurface ocean warming preceded heinrich events. Nat. Commun. 13, 4217. http://dx.doi.org/10. 1038/s41467-022-31754-x.
- McClymont, E.L., Ford, H.L., Ho, S.L., Alonso-Garcia, M., Bailey, I., Berke, M.A., Littler, K., Patterson, M.O., Petrick, B.F., Peterse, F., Ravelo, A.C., Risebrobakken, B., De Schepper, S., Swann, G.E.A., Thirumalai, K., Tierney, J.E., van der Weijst, C., White, S.M., 2020a. Sea Surface Temperature Anomalies for Pliocene Interglacial KM5c (PlioVAR). PANGAEA, http://dx.doi.org/10.1594/PANGAEA.911847.
- McClymont, E.L., Ford, H.L., Ho, S.L., Tindall, J.C., Haywood, A.M., Alonso-Garcia, M., Bailey, I., Berke, M.A., Littler, K., Patterson, M.O., Petrick, B., Peterse, F., Ravelo, A.C., Risebrobakken, B., De Schepper, S., Swann, G.E.A., Thirumalai, K., Tierney, J.E., van der Weijst, C., White, S., Abe-Ouchi, A., Baatsen, M.L.J., Brady, E.C., Chan, W.-L., Chandan, D., Feng, R., Guo, C., von der Heydt, A.S., Hunter, S., Li, X., Lohmann, G., Nisancioglu, K.H., Otto-Bliesner, B.L., Peltier, W.R., Stepanek, C., Zhang, Z., 2020b. Lessons from a high-CO<sub>2</sub> world: an ocean view from ~ 3 million years ago. Clim. the Past 16 (4), 1599–1615. http://dx.doi.org/10.5194/cp-16-1599-2020.
- McClymont, E.L., Ho, S.L., Ford, H.L., Bailey, I., Berke, M.A., Bolton, C.T., De Schepper, S., Grant, G.R., Groeneveld, J., Inglis, G.N., Karas, C., Patterson, M.O., Swann, G.E.A., Thirumalai, K., White, S.M., Alonso-Garcia, M., Anand, P., Hoogakker, B.a.A., Littler, K., Petrick, B.F., Risebrobakken, B., Abell, J.T., Crocker, A.J., de Graaf, F., Feakins, S.J., Hargreaves, J.C., Jones, C.L., Markowska, M., Ratnayake, A.S., Stepanek, C., Tangunan, D., 2023a. Climate evolution through the onset and intensification of northern hemisphere glaciation. Rev. Geophys. 61 (3), e2022RG000793. http://dx.doi.org/10.1029/2022RG000793.
- McClymont, E.L., Ho, S.L., Ford, H.L., Bailey, I., Berke, M.A., Bolton, C.T., Schepper, S.D., Grant, G.R., Groeneveld, J., Inglis, G.N., Karas, C., Patterson, M.O., Swann, G.E.A., Thirumalai, K., White, S.M., Alonso-Garcia, M., Anand, P., Hoogakker, B.A.A., Littler, K., Petrick, B.F., Risebrobakken, B., Abell, J., Crocker, A.J., Graaf, F.M.d., Feakins, S.J., Hargreaves, J.C., Jones, C.L., Markowska, M., Ratnayake, A.S., Stepanek, C., Tangunan, D.N., 2023b. Synthesis of Sea Surface Temperature and Foraminifera Stable Isotope Data Spanning the Mid-Pliocene Warm Period and Early Pleistocene (Pliovar). PANGAEA, http://dx.doi.org/10.1594/PANGAEA.956158.
- Miller, M.J., Palmer, T.N., Swinbank, R., 1989. Parametrization and influence of subgrid-scale orography in general circulation and numerical weather prediction models. Meteorol. Atmos. Phys. 40, 84–109. http://dx.doi.org/10.1007/ BF01027469.

- Naish, T., Powell, R., Levy, R., Wilson, G., Scherer, R., Talarico, F., Krissek, L., Niessen, F., Pompilio, M., Wilson, T., Carter, L., DeConto, R., Huybers, P., McKay, R., Pollard, D., Ross, J., Winter, D., Barrett, P., Browne, G., Cody, R., Cowan, E., Crampton, J., Dunbar, G., Dunbar, N., Florindo, F., Gebhardt, C., Graham, I., Hannah, M., Hansaraj, D., Harwood, D., Helling, D., Henrys, S., Hinnov, L., Kuhn, G., Kyle, P., Läufer, A., Maffioli, P., Magens, D., Mandernack, K., McIntosh, W., Millan, C., Morin, R., Ohneiser, C., Paulsen, T., Persico, D., Raine, I., Reed, J., Riesselman, C., Sagnotti, L., Schmitt, D., Sjunneskog, C., Strong, P., Taviani, M., Vogel, S., Wilch, T., Williams, T., 2009. Obliquity-paced Pliocene West Antarctic ice sheet oscillations. Nature 458 (7236), 322–328. http://dx.doi.org/10.1038/nature07867.
- Orsi, A.H., Johnson, G.C., Bullister, J.L., 1999. Circulation, mixing, and production of Antarctic bottom water. Prog. Oceanogr. 43, 55–109. http://dx.doi.org/10.1016/S0079-6611(99)00004-X.
- Otto-Bliesner, B.L., Braconnot, P., Harrison, S.P., Lunt, D.J., Abe-Ouchi, A., Albani, S., Bartlein, P.J., Capron, E., Carlson, A.E., Dutton, A., Fischer, H., Goelzer, H., Govin, A., Haywood, A., Joos, F., LeGrande, A.N., Lipscomb, W.H., Lohmann, G., Mahowald, N., Nehrbass-Ahles, C., Pausata, F.S.R., Peterschmitt, J.-Y., Phipps, S.J., Renssen, H., Zhang, Q., 2017a. The PMIP4 contribution to CMIP6 Part 2: Two interglacials, scientific objective and experimental design for Holocene and Last Interglacial simulations. Geosci. Model. Dev. 10 (11), 3979–4003. http://dx.doi.org/10.5194/gmd-10-3979-2017.
- Otto-Bliesner, B.L., Brady, E.C., Zhao, A., Brierley, C.M., Axford, Y., Capron, E., Govin, A., Hoffman, J.S., Isaacs, E., Kageyama, M., Scussolini, P., Tzedakis, P.C., Williams, C.J.R., Wolff, E., Abe-Ouchi, A., Braconnot, P., Ramos Buarque, S., Cao, J., de Vernal, A., Guarino, M.V., Guo, C., LeGrande, A.N., Lohmann, G., Meissner, K.J., Menviel, L., Morozova, P.A., Nisancioglu, K.H., O'ishi, R., Salas y Mélia, D., Shi, X., Sicard, M., Sime, L., Stepanek, C., Tomas, R., Volodin, E., Yeung, N.K.H., Zhang, Q., Zhang, Z., Zheng, W., 2021. Large-scale features of last interglacial climate: results from evaluating the lig127k simulations for the Coupled Model Intercomparison Project (CMIP6)–Paleoclimate Modeling Intercomparison Project (PMIP4). Clim. the Past 17 (1), 63–94. http://dx.doi.org/10.5194/cp-17-63-2021.
- Otto-Bliesner, B.L., Jahn, A., Feng, R., Brady, E.C., Hu, A., Löfverström, M., 2017b. Amplified North Atlantic warming in the late Pliocene by changes in Arctic gateways. Geophys. Res. Lett. 44 (2), 957–964. http://dx.doi.org/10.1002/2016GL071805.
- Pollard, D., DeConto, R.M., 2009. Modelling West Antarctic ice sheet growth and collapse through the past five million years. Nature 458 (7236), 329–332. http: //dx.doi.org/10.1038/nature07809.
- Pontes, G.M., Wainer, I., Taschetto, A.S., Gupta, A.S., Abe-Ouchi, A., Brady, E.C., Chan, W.-L., Chandan, D., Contoux, C., Feng, R., Hunter, S.J., Kame, Y., Lohmann, G., Otto-Bliesner, B.L., Peltier, W.R., Stepanek, C., Tindall, J., Tan, N., Zhang, Q., Zhang, Z., 2020. Drier tropical and subtropical Southern Hemisphere in the mid-Pliocene Warm Period. Sci. Rep. 10, 13458. http://dx.doi.org/10.1038/s41598-020-68884-5.
- Pound, M.J., Tindall, J., Pickering, S.J., Haywood, A.M., Dowsett, H.J., Salzmann, U., 2014. Late Pliocene lakes and soils: a global data set for the analysis of climate feedbacks in a warmer world. Clim. the Past 10 (1), 167–180. http://dx.doi.org/ 10.5194/cp-10-167-2014.
- Raffi, I., Wade, B.S., Pälike, H., Beu, A.G., Cooper, R., Crundwell, M.P., Krijgsman, W., Moore, T., Raine, I., Sardella, R., Vernyhorova, Y.V., 2020. Chapter 29 The neogene period. In: Gradstein, F.M., Ogg, J.G., Schmitz, M.D., Ogg, G.M. (Eds.), Geologic Time Scale 2020. Elsevier, pp. 1141–1215. http://dx.doi.org/10.1016/B978-0-12-824360-2.00029-2.
- Rahmstorf, S., 1995. Bifurcations of the Atlantic thermohaline circulation in response to changes in the hydrological cycle. Nature 378, 145–149. http://dx.doi.org/10. 1038/378145a0.
- Raymo, M.E., Mitrovica, J.X., O'Leary, M.J., DeConto, R.M., Hearty, P.J., 2011. Departures from eustasy in Pliocene sea-level records. Nat. Geosci. 4 (5), 328–332. http://dx.doi.org/10.1038/ngeo1118.
- Ren, X., Lunt, D.J., Hendy, E., von der Heydt, A., Abe-Ouchi, A., Otto-Bliesner, B., Williams, C.J.R., Stepanek, C., Guo, C., Chandan, D., Lohmann, G., Tindall, J.C., Sohl, L.E., Chandler, M.A., Kageyama, M., Baatsen, M.L.J., Tan, N., Zhang, Q., Feng, R., Hunter, S., Chan, W.-L., Peltier, W.R., Li, X., Kamae, Y., Zhang, Z., Haywood, A.M., 2023. The hydrological cycle and ocean circulation of the Maritime Continent in the Pliocene: results from PlioMIP2. Clim. the Past 19 (10), 2053–2077. http://dx.doi.org/10.5194/cp-19-2053-2023.
- Roeckner, E., Bäuml, G., Bonaventura, L., Brokopf, R., Esch, M., Giorgetta, M., Hagemann, S., Kirchner, I., Kornblueh, L., Manzini, E., Rhodin, A., Schlese, U., Schulzweida, U., Tompkins, A., 2003. The atmospheric general circulation model ECHAM 5. PART I: model description. Max Planck Inst. Meteorol. Rep. 349.
- Rowley, D.B., Forte, A.M., Moucha, R., Mitrovica, J.X., Simmons, N.A., Grand, S.P., 2013. Dynamic topography change of the Eastern United States since 3 million years ago. Science 340 (6140), 1560–1563. http://dx.doi.org/10.1126/science. 1229180.
- Salzmann, U., Dolan, A.M., Haywood, A.M., Chan, W.-L., Voss, J., Hill, D.J., Abe-Ouchi, A., Otto-Bliesner, B., Bragg, F.J., Chandler, M.A., Contoux, C., Dowsett, H.J., Jost, A., Kamae, Y., Lohmann, G., Lunt, D.J., Pickering, S.J., Pound, M.J., Ramstein, G., Rosenbloom, N.A., Sohl, L., Stepanek, C., Ueda, H., Zhang, Z.,

- 2013. Challenges in quantifying Pliocene terrestrial warming revealed by data-model discord. Nat. Clim. Chang. 3 (11), 969–974. http://dx.doi.org/10.1038/nclimate2008
- Salzmann, U., Haywood, A.M., Lunt, D.J., Valdes, P.J., Hill, D.J., 2008. A new global biome reconstruction and data-model comparison for the Middle Pliocene. Glob. Ecol. Biogeogr. 17 (3), 432–447. http://dx.doi.org/10.1111/j.1466-8238.
- Savita, A., Kjellsson, J., Pilch Kedzierski, R., Latif, M., Rahm, T., Wahl, S., Park, W., 2024. Assessment of climate biases in OpenIFS version 43r3 across model horizontal resolutions and time steps. Geosci. Model. Dev. 17, 1813–1829. http://dx.doi.org/ 10.5194/gmd-17-1813-2024.
- Scafetta, N., 2022. Advanced testing of low, medium, and high ECS CMIP6 GCM simulations versus ERA5-t2m. Geophys. Res. Lett. 49 (6), e2022GL097716. http://dx.doi.org/10.1029/2022GL097716.
- Scholz, P., Sidorenko, D., Danilov, S., Wang, Q., Koldunov, N., Sein, D., Jung, T., 2022. Assessment of the finite-volume sea ice-ocean model (FESOM2.0) - Part 2: Partial bottom cells, embedded sea ice and vertical mixing library CVMix. Geosci. Model. Dev. 15 (2), 335–363. http://dx.doi.org/10.5194/gmd-15-335-2022.
- Scholz, P., Sidorenko, D., Gurses, O., Danilov, S., Koldunov, N., Wang, Q., Sein, D., Smolentseva, M., Rakowsky, N., Jung, T., 2019. Assessment of the finite-volume sea ice-ocean model (FESOM2.0) Part 1: Description of selected key model elements and comparison to its predecessor version. Geosci. Model. Dev. 12 (11), 4875–4899. http://dx.doi.org/10.5194/gmd-12-4875-2019.
- Schulzweida, U., 2023. CDO User Guide. Zenodo, http://dx.doi.org/10.5281/zenodo. 10020800.
- Shankle, M.G., Burls, N.J., Fedorov, A.V., Thomas, M.D., Liu, W., Penman, D.E., Ford, H.L., Jacobs, P.H., Planavsky, N.J., Hull, P.M., 2021. Pliocene decoupling of equatorial Pacific temperature and pH gradients. Nature 598, 457–461. http://dx.doi.org/10.1038/s41586-021-03884-7.
- Shepard, D., 1968. A two-dimensional interpolation function for irregularly-spaced data. In: Proceedings of the 1968 23rd ACM National Conference. ACM '68, Association for Computing Machinery, New York, NY, USA, pp. 517–524. http: //dx.doi.org/10.1145/800186.810616.
- Steele, M., Morley, R., Ermold, W., 2001. PHC: A global ocean hydrography with a high-quality Arctic ocean. J. Clim. 14, 2079–2087. http://dx.doi.org/10.1175/1520-0442(2001)014<2079:PAGOHW>2.0.CO;2.
- Stepanek, C., Samakinwa, E., Knorr, G., Lohmann, G., 2020. Contribution of the coupled atmosphere–ocean–sea ice–vegetation model COSMOS to the PlioMIP2. Clim. the Past 16, 2275–2323. http://dx.doi.org/10.5194/cp-16-2275-2020.
- Stevens, B., Giorgetta, M., Esch, M., Mauritsen, T., Crueger, T., Rast, S., Salzmann, M., Schmidt, H., Bader, J., Block, K., Brokopf, R., Fast, I., Kinne, S., Kornblueh, L., Lohmann, U., Pincus, R., Reichler, T., Roeckner, E., 2013. Atmospheric component of the MPI-M Earth System Model: ECHAM6. J. Adv. Model. Earth Syst. 5 (2), 146–172. http://dx.doi.org/10.1002/jame.20015.
- Stommel, H., 1961. Thermohaline convection with two stable regimes of flow. Tellus 13, 224–230. http://dx.doi.org/10.1111/j.2153-3490.1961.tb00079.x.
- Streffing, J., 2020. AWI-CM3 model documentation. https://awi-cm3-documentation.readthedocs.io/en/latest/ (Accessed 9 June 2025).
- Streffing, J., 2021. ocp-tool2: A tool for ocean preprocessor files. https://github.com/ AWI-ESM/ocp-tool2 (Accessed 9 June 2025).
- Streffing, J., Sidorenko, D., Semmler, T., Zampieri, L., Scholz, P., Andrés-Martínez, M., Koldunov, N., Rackow, T., Kjellsson, J., Goessling, H., Athanase, M., Wang, Q., Hegewald, J., Sein, D.V., Mu, L., Fladrich, U., Barbi, D., Gierz, P., Danilov, S., Juricke, S., Lohmann, G., Jung, T., 2022. AWI-CM3 coupled climate model: description and evaluation experiments for a prototype post-CMIP6 model. Geosci. Model. Dev. 15 (16), 6399-6427. http://dx.doi.org/10.5194/gmd-15-6399-2022.
- Sun, Y., Ramstein, G., Contoux, C., Zhou, T., 2013. A comparative study of large-scale atmospheric circulation in the context of a future scenario (RCP4.5) and past warmth (mid-Pliocene). Clim. the Past 9 (4), 1613–1627. http://dx.doi.org/10.5194/cp-9-1613-2013.
- Sun, Y., Ramstein, G., Li, L.Z.X., Contoux, C., Tan, N., Zhou, T., 2018. Quantifying east Asian summer monsoon dynamics in the ECP4.5 scenario with reference to the mid-Piacenzian warm period. Geophys. Res. Lett. 45 (22), 12523–12533. http://dx.doi.org/10.1029/2018GL080061.
- Sun, Y., Wu, H., Ding, L., Chen, L., Stepanek, C., Zhao, Y., Tan, N., Su, B., Yuan, X., Zhang, W., Liu, B., Hunter, S., Haywood, A., Abe-Ouchi, A., Otto-Bliesner, B., Contoux, C., Lunt, D.J., Dolan, A., Chandan, D., Lohmann, G., Dowsett, H., Tindall, J., Baatsen, M., Peltier, W.R., Li, Q., Feng, R., Salzmann, U., Chan, W.-L., Zhang, Z., Williams, C.J.R., Ramstein, G., 2024. Decomposition of physical processes controlling EASM precipitation changes during the mid-Piacenzian: new insights into data-model integration. Npj Clim. Atmospheric Sci. 7, 120. http://dx.doi.org/10.1038/s41612-024-00668-4.

- Tan, N., Contoux, C., Ramstein, G., Sun, Y., Dumas, C., Sepulchre, P., Guo, Z., 2020. Modeling a modern-like pCO<sub>2</sub> warm period (Marine Isotope Stage KM5c) with two versions of an Institut Pierre Simon Laplace atmosphere-ocean coupled general circulation model. Clim. the Past 16, 1–16. http://dx.doi.org/10.5194/cp-16-1-2020
- Tierney, J.E., King, J., Osman, M.B., Abell, J.T., Burls, N.J., Erfani, E., Cooper, V.T., Feng, R., 2025. Pliocene warmth and patterns of climate change inferred from paleoclimate data assimilation. AGU Adv. 6 (1), e2024AV001356. http://dx.doi. org/10.1029/2024AV001356.
- Tierney, J.E., Poulsen, C.J., Montañez, I.P., Bhattacharya, T., Feng, R., Ford, H.L., Hönisch, B., Inglis, G.N., Petersen, S.V., Sagoo, N., Tabor, C.R., Thirumalai, K., Zhu, J., Burls, N.J., Foster, G.L., Goddéris, Y., Huber, B.T., Ivany, L.C., Kirtland Turner, S., Lunt, D.J., McElwain, J.C., Mills, B.J.W., Otto-Bliesner, B.L., Ridgwell, A., Zhang, Y.G., 2020. Past climates inform our future. Science 370 (6517), eaay3701. http://dx.doi.org/10.1126/science.aay3701.
- Tindall, J.C., Haywood, A.M., Salzmann, U., Dolan, A.M., Fletcher, T., 2022. The warm winter paradox in the Pliocene northern high latitudes. Clim. the Past 18, 1385–1405. http://dx.doi.org/10.5194/cp-18-1385-2022.
- Valcke, S., 2013. The OASIS3 coupler: a European climate modelling community software. Geosci. Model. Dev. 6 (2), 373–388. http://dx.doi.org/10.5194/gmd-6-373-2013.
- Weiffenbach, J.E., Baatsen, M.L.J., Dijkstra, H.A., von der Heydt, A.S., Abe-Ouchi, A., Brady, E.C., Chan, W.-L., Chandan, D., Chandler, M.A., Contoux, C., Feng, R., Guo, C., Han, Z., Haywood, A.M., Li, Q., Li, X., Lohmann, G., Lunt, D.J., Nisancioglu, K.H., Otto-Bliesner, B.L., Peltier, W.R., Ramstein, G., Sohl, L.E., Stepanek, C., Tan, N., Tindall, J.C., Williams, C.J.R., Zhang, Q., Zhang, Z., 2023. Unraveling the mechanisms and implications of a stronger mid-Pliocene Atlantic Meridional Overturning Circulation (AMOC) in PlioMIP2. Clim. the Past 19 (1), 61–85. http://dx.doi.org/10.5194/cp-19-61-2023.
- Weiffenbach, J.E., Dijkstra, H.A., von der Heydt, A.S., Abe-Ouchi, A., Chan, W.-L., Chandan, D., Feng, R., Haywood, A.M., Hunter, S.J., Li, X., Otto-Bliesner, B.L., Peltier, W.R., Stepanek, C., Tan, N., Tindall, J.C., Zhang, Z., 2024. Highly stratified mid-Pliocene Southern Ocean in PlioMIP2. Clim. the Past 20 (4), 1067–1086. http://dx.doi.org/10.5194/cp-20-1067-2024.
- Williams, C.J.R., Sellar, A.A., Ren, X., Haywood, A.M., Hopcroft, P., Hunter, S.J., Roberts, W.H.G., Smith, R.S., Stone, E.J., Tindall, J.C., Lunt, D.J., 2021. Simulation of the mid-Pliocene Warm Period using HadGEM3: experimental design and results from model–model and model–data comparison. Clim. the Past 17 (5), 2139–2163. http://dx.doi.org/10.5194/cp-17-2139-2021.
- Yang, Z.-L., Dickinson, R.E., 1996. Description of the biosphere-atmosphere transfer scheme (BATS) for the soil moisture workshop and evaluation of its performance. Glob. Planet. Change 13 (1), 117–134. http://dx.doi.org/10.1016/0921-8181(95) 00041-0.
- Zhang, Q., Berntell, E., Axelsson, J., Chen, J., Han, Z., de Nooijer, W., Lu, Z., Li, Q., Zhang, Q., Wyser, K., Yang, S., 2021a. Simulating the mid-Holocene, last interglacial and mid-Pliocene climate with EC-Earth3-LR. Geosci. Model. Dev. 14 (2), 1147–1169. http://dx.doi.org/10.5194/gmd-14-1147-2021.
- Zhang, R., Jiang, D., Liu, S., Zhang, C., Zhang, Z., Li, X., Tian, Z., Shi, J., 2024. Less dryland aridity during pliocene warmth. J. Geophys. Res.:Atmospheres 129, e2023JD039371. http://dx.doi.org/10.1029/2023JD039371.
- Zhang, Z., Li, X., Guo, C., Otterå, O.H., Nisancioglu, K.H., Tan, N., Contoux, C., Ramstein, G., Feng, R., Otto-Bliesner, B.L., Brady, E., Chandan, D., Peltier, W.R., Baatsen, M.L.J., von der Heydt, A.S., Weiffenbach, J.E., Stepanek, C., Lohmann, G., Zhang, Q., Li, Q., Chandler, M.A., Sohl, L.E., Haywood, A.M., Hunter, S.J., Tindall, J.C., Williams, C., Lunt, D.J., Chan, W.-L., Abe-Ouchi, A., 2021b. Midpliocene atlantic meridional overturning circulation simulated in PlioMIP2. Clim. the Past 17, 529-543. http://dx.doi.org/10.5194/cp-17-529-2021.
- Zhang, K., Sun, Y., Jiang, Y., Guo, H., Lin, J., Chen, J., Wang, X., 2025. Tropical circulation shifts and regional climate impacts: Comparing mid-Piacenzian warmth and future warming (SSP2-4.5). Glob. Planet. Change 253, 104941. http://dx.doi. org/10.1016/j.gloplacha.2025.104941.
- Zheng, J., Zhang, Q., Li, Q., Zhang, Q., Cai, M., 2019. Contribution of sea ice albedo and insulation effects to Arctic amplification in the EC-Earth Pliocene simulation. Clim. the Past 15 (1), 291–305. http://dx.doi.org/10.5194/cp-15-291-2019.
- Zubakov, V.A., Borzenkova, I.I., 1988. Pliocene palaeoclimates: Past climates as possible analogues of mid-twenty-first century climate. Palaeogeogr. Palaeoclimatol. Palaeoecol. 65 (1), 35–49. http://dx.doi.org/10.1016/0031-0182(88)90110-1.